XMM-Newton

XMM-Newton Science Analysis System (version 6.0)
Science Validation Report

XMM-SOC-USR-TN-0009 Issue 1.1

M. Guainazzi, C.Gabriel, B.Altieri, B.Chen, M.Ehle, M.Kirsch, A.Pollock, R.Saxton, A.Talavera
XMM-Newton Science Operations Center

J.Osborne, M.Denby, I.Stewart
XMM-Newton Science Survey Center

14 April 2004

Revision history

Revision number	Date	Revision author	Comments
0.1	29 January 2004	M.Guainazzi	LATEX template
0.2	5 March 2004	M.Guainazzi	First complete draft
0.3	15 March 2004	M.Guainazzi	Second complete draft (after SOC/SSC-LUX comments)
0.4	23 March 2004	M.Guainazzi	Third complete draft (after SOC/SSC comments)
1.0	24 March 2004	M.Guainazzi	Public version
1.1	14 April 2004	M.Guainazzi	Minor editorial changes

Contents

1 Introduction **1**
1.1 Concept . . . 1
1.2 Methodology . . . 1

2 Pipeline (PPS) validation **3**

3 OM grism processing **3**
3.1 Obs.#0125911301: HD 13499 . . . 4
3.2 Obs.#0125910901: HZ 2 . . . 4

4 SAS interactive tasks validation **7**
4.1 `arfgen` . . . 7
4.2 `lccorr` . . . 7
4.3 `omsource` . . . 7
4.4 `omgsource` . . . 8

5 Calibration items **8**
5.1 EPIC astrometry . . . 8
5.1.1 EPIC relative astrometry . . . 9
5.1.2 EPIC absolute astrometry . . . 9
5.2 EPIC cameras effective area . . . 11
5.2.1 PKS0558-504, Obs.#0125110101, Rev.#84 . . . 11
5.2.2 PKS0558-504, Obs.#0129360201, Rev.#153 . . . 12
5.2.3 G21.5-0.9 . . . 17
5.2.4 Her X-1 – pn Timing mode . . . 20
5.2.5 Crab – pn Burst mode . . . 20
5.2.6 On the relative normalization among the EPIC cameras . . . 21
5.3 EPIC cameras timing . . . 22
5.4 MOS Timing Mode CTI correction . . . 23
5.5 OM filter photometry . . . 26
5.6 OM astrometry . . . 26
5.7 OM grisms wavelength scale and flux calibration . . . 28
5.8 OM Fast Mode timing accuracy . . . 29
5.9 RGS effective area . . . 30
5.9.1 Pixel-by-pixel offset subtraction . . . 32
5.10 RGS wavelength scale . . . 33

6 XMM-Newton instrument cross-calibration **33**

7 Conclusions **37**

1 Introduction

1.1 Concept

Scientific Validation (SV) is required in order to ensure a constant high quality of the XMM-Newton Science Analysis System (SAS).
The main purpose of the SV is to provide the SAS community with a stable reliable software product, as well as to generate a list of caveats and known deficiencies. Together with these "functional" tests, the SV provides some information on the expected systematic uncertainties when basic data analysis products are generated through the current version of the SAS, using the best calibrations available at the moment SAS was released. It is important to stress that *this document does not supersede or substitute* the **instrument calibration status documents**, available from the XMM-Newton calibration portal. Instrument calibration is a continuous activity, whose results (update of calibration files) is intrinsically and necessarily decoupled from software releases. XMM-Newton users are recommended to consult periodically the URL: `http://xmm.vilspa.esa.es/calibrations`, which informs on the calibration status of the XMM-Newton instruments.
The document you are reading (*SAS Science Validation Report*) contains information about:

- which instrumental modes are fully supported by SAS,
- which scientific products SAS can produce,
- the level of accuracy associated with those products,
- a list of caveats and problems.

The SV is performed on a standard set of XMM-Newton observations, which cover all commissioned observational modes. Tab. 1 lists all the datasets used for the validation of SAS version 6.0 (*SAS v6.0* hereinafter). Some of these observations are particularly suitable to test calibration-related items, as specified in the rightmost column of Tab. 1. These datasets are intended as a standard reference, which has been and will be used to verify the performances of all SAS versions. However, additional datasets may occasionally be used to test version-specific SAS items. This is the case, for instance, for the datasets discussed in Sect. 5.4 of this report. Datasets discussed in a given report and not listed in Tab. 1 do not belong to the reference datasets, and are therefore not intended to be discussed in later SAS versions validation reports.

1.2 Methodology

The SV for SAS v6.0 consisted of the following steps:

1. all the SV datasets were processed through the Pipeline Product System (PPS) at the Science Survey Center (SSC). A summary of the results of the PPS processing is reported in Sect. 2
2. the same datasets are also processed through the SAS reduction meta-tasks: `e[mp]proc`, `om[ifg]chain`, `rgsproc`
3. products generated by steps 1 and 2 above are used as basis for the *interactive SV analysis*. Standard scientific products (images, light curves, spectra, source lists) are generated and analyzed. This allows to:

Table 1: SV datasets

Instrument	Mode	Object	Revolution Observation ID	Dataset ID	Calibration item
EPIC MOS	Full Frame	Lockman Hole	070 0123700101	1	Astrometry
	"	G21.5.09	060 0122700101	2	Effective area
	Small Window (W2)	Mkn 421	165 0099280201	3	
	Large Window (W3)	PKS0558-504	153 0129360201	4	Effective area
	Timing Uncompressed	Her X-1	207 0134120101	5	Timing
EPIC-pn	Full Frame	Lockman Hole	070 0123700101	1	Astrometry
	Full Frame/Small Window	PKS0558-504	153 0129360201	4	Effective area
	Large Window	AB Dor	185 0133120201	6	
	Small Window	PKS0558-504	084 0125110101	7	Effective area
	Fast Timing	Her X-1	207 0134120101	5	Timing
		Crab	411 0153750401	8	
	Fast Burst	Crab	411 0153750301	9	Timing
		Crab	411 0153750501	10	Timing
	Extended Full Frame	G21.5-0.9	060 0122700101	2	Effective area
RGS	SPEC+Q	PKS0558-504	084 0125110101	7	
"		Mkn 421	165 0099280201	3	Effective area
	"	AB Dor	185 0133120201	6	Wavelength scale
	"	AB Dor	338 0134521301	11	Wavelength scale
	"	AB Dor	462 0134521601	12	Wavelength scale
	"	AB Dor	572 0134522201	13	Wavelength scale
OM	Image Mode	BPM 16274	261 0125320701	14	Photometry
	Fast Mode	X1822-371	228 0111230101	15	
	FF Low Resolution	BPM 16274	261 0125320701	14	Astrometry
	Optical grism	Hz2	503 0125910901	16	Wavelength scale & flux calibration
	UV Grism	HD13499 (offset)	657 0125911301	17	Wavelength scale & flux calibration

- test the SAS interactive tasks. A summary of these tests is reported in Sect. 4
- verify the calibration accuracy obtained with SAS v6.0, and compare it with the expected accuracy on the basis of the calibration status at the time the SV is performed. Results of this analysis are reported in Sect. 5

The conclusions of the SV are summarized in Sect. 7. A list of instrument modes supported by SAS v6.0 is reported in Appendix A. A summary of SAS v6.0 capabilities is detailed in Appendix B.
In this report: best-fit parameter uncertainties are at the 90% confidence level for 1 interesting parameter ($\Delta\chi^2 = 2.71$); errors on positions or count rates are at the 1-σ level; energies are quoted in the observer's reference frame unless otherwise specified.

2 Pipeline (PPS) validation

All SV datasets were nominally processed by the PPS. Science results yielded by the PPS - or extracted from event lists produced by the PPS - are almost identical to those obtained through the run of the SAS v6.0 reduction meta-tasks. Remaining differences can be entirely explained as due to the different data screening criteria and software configurations employed by the PPS pipeline and the SAS reduction meta tasks (see, *e.g.*, Sect. 5.2.2, and Sect. 5.2.3).
Users can access the PPS products for the SV datasets through the XMM-Newton Science Archive (XSA) user interface (`http://xmm.vilspa.esa.es/xsa`). PPS products can be accessed as a whole, or per product group category (using the `CUSTOM` option in the XSA). Users are referred to the "Guided Tour to the XSA"
(`http://xmm.vilspa.esa.es/external/xmm_data_acc/xsa/docs/tour.shtml`) for instructions on how to access the XSA content.

3 OM grism processing

SAS v6.0 contains for the first time utilities to reduce and analyze data obtained with the OM grisms. A new chain, `omgchain`, has been designed to fully extract and automatically calibrate the spectra produced by OM grisms. Some of its modules are common to the already existing OM Image Mode data chain, others are grism specific and perform the spectral extraction and the wavelength and flux calibration as well as plotting the results.
A new interactive task, `omgsource`, allows the user to select with the cursor the spectrum to be extracted.
OM grism spectra can be registered by a user defined window encompassing the spectrum of the target located at the boresight, or including the spectra of all targets in the field of view in Full Frame Low Resolution Mode. SAS handles these two cases in the same way, although in the latter, the four image files composing the whole image are combined prior to starting any other task.
The initial SSC pipeline using SAS v6.0 will not make OM grism products. This function will be added when confidence in fully automated analysis is established.
The processing of grism data with SAS has the following steps:

- **image preparation**

  As in all OM image mode data, `omprep` and `ommodmap` are run to extract information from the tracking history and house-keeping files, and to add it to the header. A "modulo-8" correction is also performed on the grism image.

- **distortion correction and rotation**

  The grism image is corrected for geometric distortion of the detector and rotated, so as to have the dispersion direction (the spectra) aligned with the image Y axis. The task `omgprep` achieves this.

- **detection of spectra**

  `omdetect` searches the whole image for spectra, both zero and first orders. A source list is generated with all successful detections.

- **spectral extraction and calibration**

  `omgrism` first analyzes the detections in the source list to establish relations among detected zero orders and the corresponding first orders. Then a boxcar extraction is performed on the successful relations. The extracted spectra are calibrated in wavelength and flux. In case a relation cannot be found for well defined zero orders, a default extraction is used for the zero order. The final spectra are written in a FITS file.

- **plotting**

  `omgrismplot` produces plots of the spectra (net spectrum, background and flux calibrated) in PDF and PS formats.

3.1 Obs.#0125911301: HD 13499

HD 13499 is a F5V star. It has been observed several times as wavelength calibrator. In the field of view, there is also HD 13434 (F7V). This observation was performed by off-setting the main target so as to have the spectra of both stars in a Full Frame Low Resolution exposure. Only the UV grism was used, because both stars are too bright for the Visible grism.
`omgchain` was run on this observation. The results of `omdetect` are shown in Fig.1. The spectra of the two bright stars (first order) were detected as well as a few other spectra. The proper detection of the zero order is made difficult by their extreme brightness. One of them is not properly detected due to a close-by straylight feature. The background is very inhomogeneous due to straylight, and this produces many spurious detections.
`omgrism` is able to extract the spectra of the two stars, although the incorrect detection of the zero order for one of them produces a shift in its wavelength scale. (See Fig. 2, where the extracted net spectra and background are presented in count-rate versus wavelength.)

3.2 Obs.#0125910901: HZ 2

HZ 2 is a standard white dwarf. It is one of the standard candles used to derive the flux calibration of the grisms. It was observed several times by XMM-Newton. This ODF is used to check the consistency of the whole SAS processing of OM grism.
The observation was performed in User Defined mode. Fig. 3 shows the results of `omdetect` in the Visible and UV grism images, after running `omgchain`. The target spectra are detected in both grisms together with some other zero orders. Faint spectra (first order) are not detected. `omgrism` fails in relating the detected zero and first orders in the Visible grism and the default extraction is applied.
For the UV grism, `omdetect` finds some features in the place of the target's first order spectrum, but it is unable to recognize the whole order as such. Again the default extraction is applied to the target's zero order.

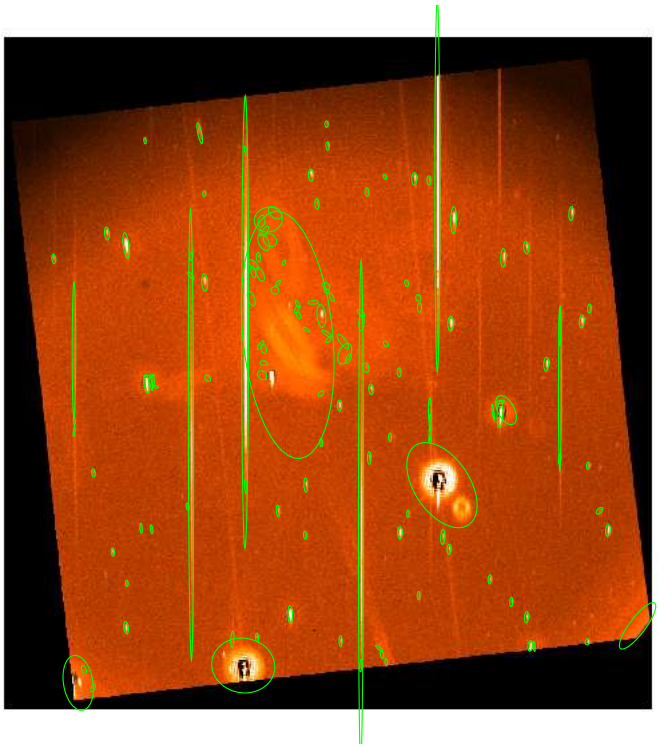

Figure 1: Detection of spectra obtained with the OM UV grism in the HD 13499 field (the bright object on the mid-right part of the image)

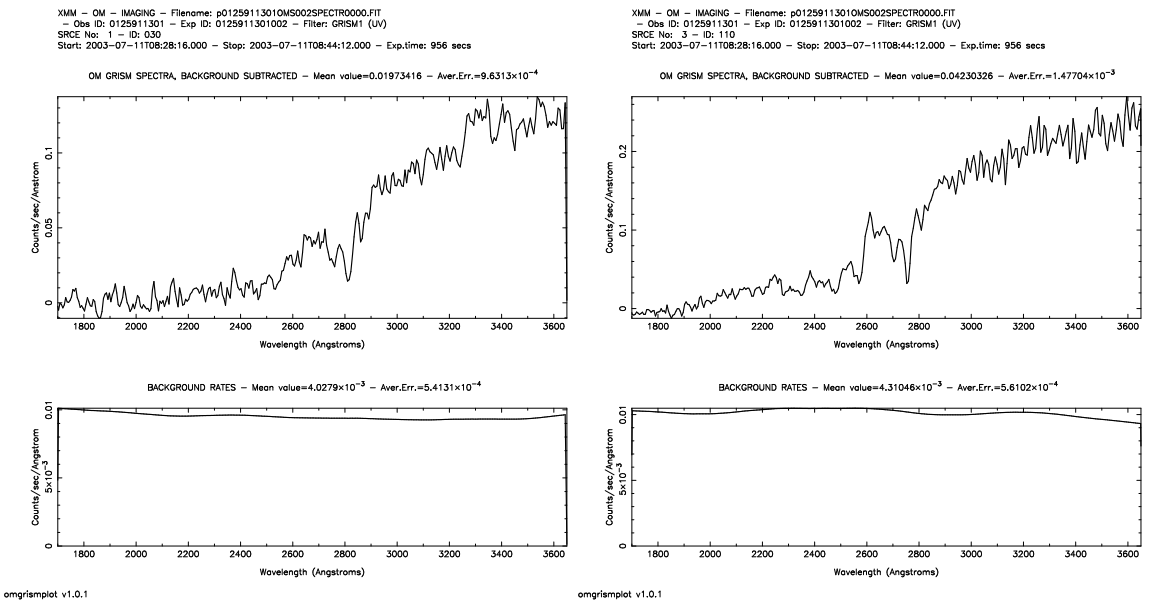

Figure 2: *Right panel*: extracted UV spectrum of HD 13434; *Left panel*: extracted UV spectrum of HD 13499. Note the wavelength shift in the Mg II lines at 2800 Å

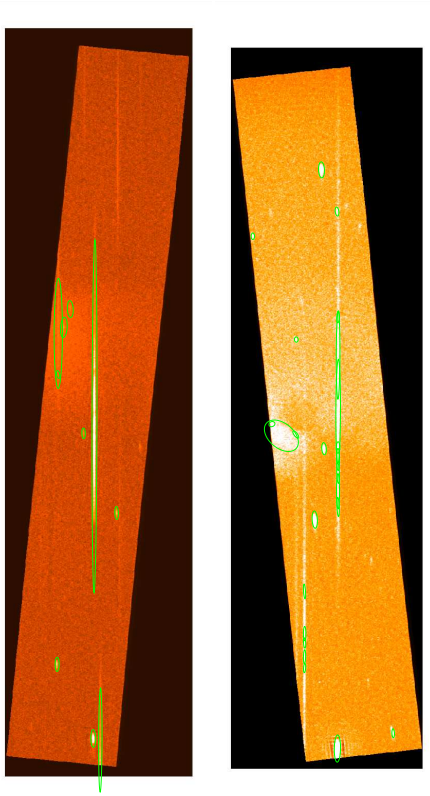

Figure 3: Detection of spectra in HZ 2. *Left*: Visible grism. *Right*: UV grism

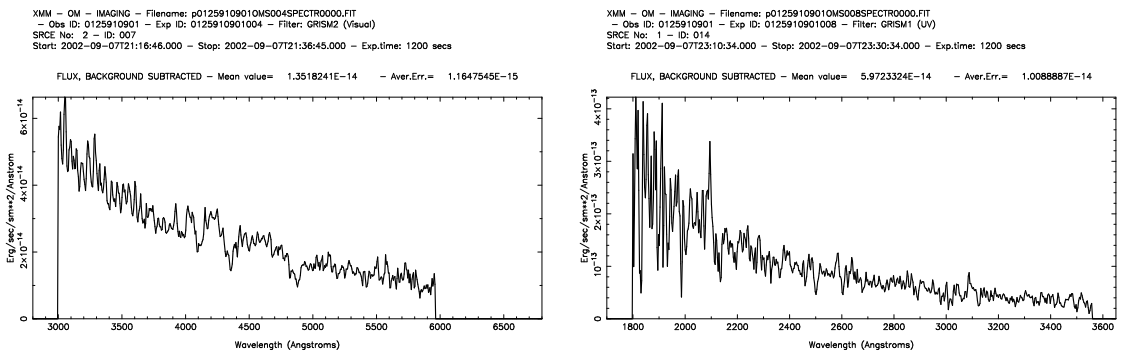

Figure 4: Flux calibrated Visible (*left panel*), and UV (*right panel*) grism spectra of HZ 2

The flux calibrated spectra of HZ 2 are presented in Fig. 4. The Visible spectrum shows clearly some hydrogen lines. The ripple features in both spectra are due to residual "modulo-8" pattern present in the image, which cannot be entirely corrected by `ommodmap`.

4 SAS interactive tasks validation

The following tasks have been tested during the SAS interactive tasks validation: `arfgen`, `backscale`, `[earth]barycen`, `edetect_chain` (with its component modules), `especget`, `ev/xmmselect`, `lccorr`, `odfbrowser`, `omsource`, `omgsource`, `rgsrmfgen`, `rgsfluxer`, `rmfgen`, `srcdisplay`. They generally exhibit a fully nominal behavior. In the following, remarks are given on individual tasks, whenever appropriate. A continuously updated list of known SAS bugs and limitations is provided by the "watchout and evergreen tips" web page at the URL: `http://xmm.vilspa.esa.es/sas/documentation/watchout`.

4.1 `arfgen`

The tests described in Sect. 5.2.3 underlines the importance that `arfgen` is provided (via a "detector map") with the most accurate description of the source spatial extent, even in the case of moderately extended, nominally on-axis sources.

4.2 `lccorr`

The light-curve manipulation task `lccorr` has undergone a substantial revision with SAS v6.0. With the SAS v6.0 version, processing of light curve extracted from pn event lists in Imaging Mode data is possible. Timing Mode in either MOS or pn is, however, not supported yet. Although the current version has been significantly tested before release, users are recommended to verify carefully the scientific results obtained with `lccorr`, given the extent of the modifications introduced with this new version.

4.3 `omsource`

`omsource` is an interactive SAS task which performs interactive photometry with OM. This task works on SAS processed images (after flat-field and "modulo 8" corrections). We have tested `omsource` using BPM16271 observations in Full Frame Low Resolution mode. The task exhibits

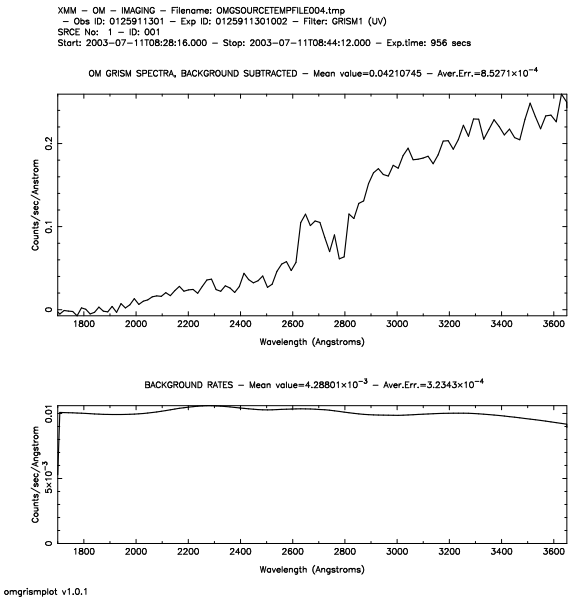

Figure 5: Interactively extracted UV grism spectrum of HD 13499

a nominal behavior. User may consider to tune the photometry, after changing the aperture radius and background annulus. This is sometimes necessary when the targets are significantly affected by the straylight features, or the field is very crowded.

4.4 `omgsource`

The interactive grism extraction task `omgsource` has been used in the data of HD 13499 and HZ 2. The same spectra automatically extracted by `omgchain` have been selected and compared. The interactively extracted spectrum of HD 13499 (see Fig. 2) is presented in Fig. 5. Since the zero order centroiding is constrained by the selection done with the cursor and not by the fake detection provided by `omdetect`, the wavelength scale appears now without shift.

5 Calibration items

5.1 EPIC astrometry

The astrometry on the Lockman Hole observation in Rev.#70 has been revisited with SAS v6.0 and new CCFs: BORESIGHT 17 and MISCDATA 20[1]. Both CCFs have been introduced with SAS v6.0 to support a better calibration of the vignetting for the three cameras. The position where the optical axis intercepts the focal plane has been changed in MISCDATA, and hence the Euler misalignment angles in the BORESIGHT CCFs. This has obviously an impact on the absolute astrometry. The new misalignment angles were calculated from the OMC2/3 rich stellar field.

The `edetect_chain` SAS meta-task was run on event lists generated with the `e[mp]chain` pipeline to get source lists for the three cameras. The sky coordinates of the sources were

[1]We stress that SAS v6.0 requires the usage of the most updated calibration files. In particular, users are strongly recommended not to use old BORESIGHT and MISCDATA CCF with SAS v6.0

cross-correlated with the (most likely) optical counterparts coordinates (Lehmann et al. 2001). Most of the sources are point-like AGN, that were already detected by ROSAT.

5.1.1 EPIC relative astrometry

The relative astrometry accuracy can be assessed from Fig. 6. The error scatter is essentially similar in SAS v6.0 and SAS v5.4, somewhat better for the MOS cameras, somewhat worse for the pn. This indicates that that within errors there is no measurable degradation of relative astrometry on this field, that could have been introduced by an imperfect roll angle rotation (Euler ψ angle in the BORESIGHT CCF).
Once the global shift of the XMM frame to the optical reference frame is applied, the mean error (scatter) from the X-ray position to the optical is the same for the 3 cameras: $1.8''$ (1σ) , or $1.3''$ (1σ) per axis. These values are probably upper limits as :

1. some cross-identifications are probably wrong at the edge of the cross-correlation radius used here ($5''$).
2. the optical coordinates have a limited accuracy (about $0.3''$)
3. coordinates of the faint EPIC sources have uncertainties due to the statistical accuracy of the measurement. This source of error is not taken into account here; however, the SAS task `eposcorr` would

The relative astrometry accuracy could be further degraded for the MOS cameras, as some systematic offsets between MOS CCDs have been detected, that ought to be corrected in the LINCOORD CCFs. Analysis is on-going on several stellar fields to determine the amount of this correction.
A possible residual in roll angle rotation could be refined, after the LINCOORD CCFs are optimized.

5.1.2 EPIC absolute astrometry

Analysis of a later (Rev.#548) observation of the same field indicates that the global astrometry offset is $1.2''$ only for the three cameras, *i.e.* close to the typical absolute astrometry accuracy observed since. Nonetheless, in this report we still quote the results obtained on the Rev.#70 Lockman Hole observation for comparison with previous SAS Science Validation reports.
The results are shown in Fig. 6 for MOS1, MOS2 and pn. An offset of about 2.5–$3''$ for the 3 cameras is clearly seen, mostly in the right ascension direction. The amplitude of the offsets were similar in SAS v5.4 (BORESIGHT 16), except may be for MOS2 where they are a little larger with SAS v6.0.
This shift from the XMM-Newton reference frame is high, but still consistent with the absolute XMM-Newton astrometry accuracy of $2''$ (1σ). This could be due to the fact that the attitude history file for such an old observation was generated with an early version of the attitude reconstruction software. This software has largely improved later-on.
A mean difference of $1.6''$ (in declination) between MOS1 and pn is evidenced again on this observation with SAS v6.0. Such a difference was already present with the previous set of CCFs in SAS v5.4 ($1.9''$). It is worth noticing that this shift is not systematically confirmed on other fields.
Hence the absolute astrometry in SAS v6.0 is consistent with SAS v5.4 within the statistical uncertainties, although slightly different from the latter, as expected.

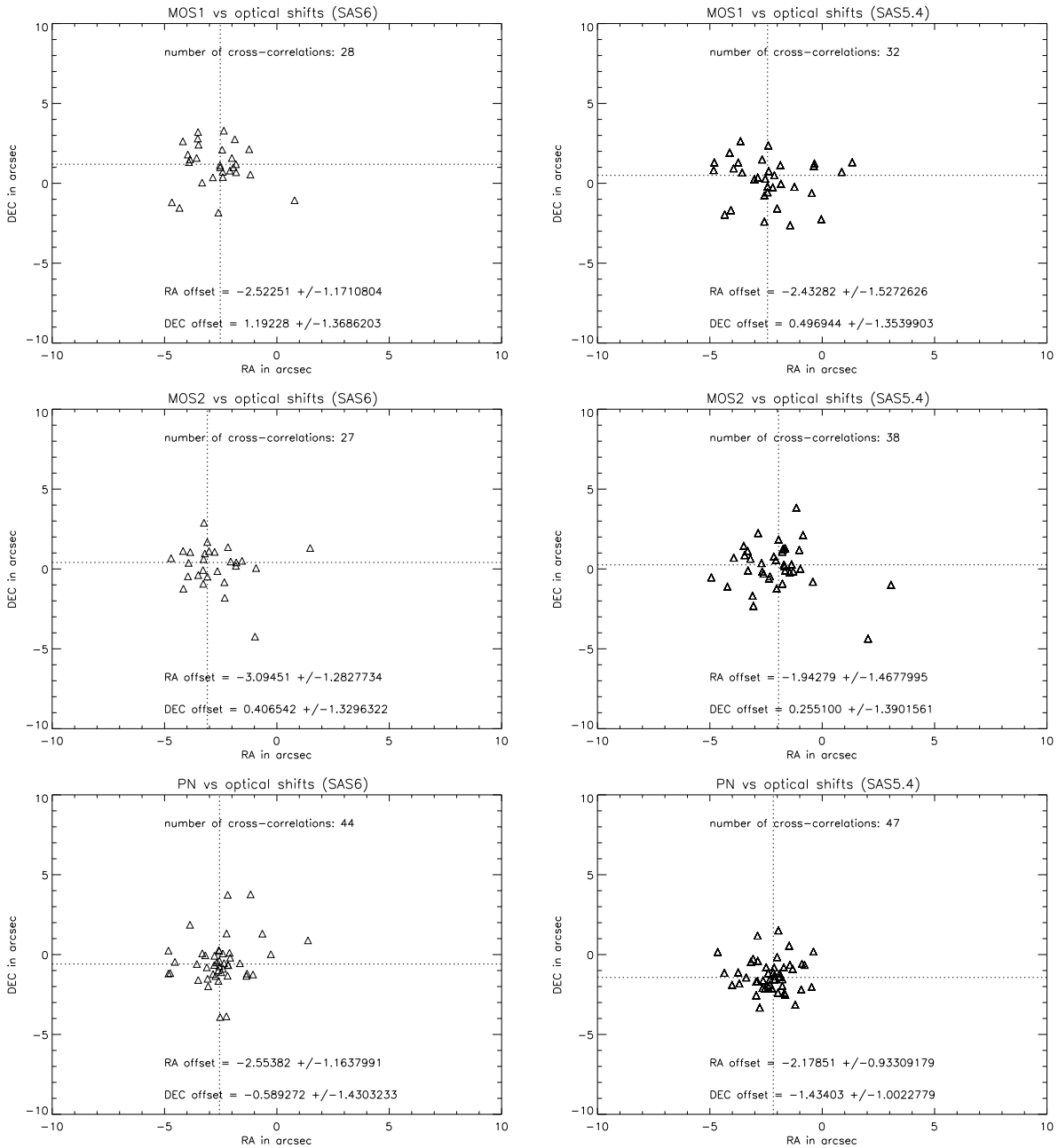

Figure 6: Offsets of sky coordinates between EPICs and optical counterparts, with a cross-correlation radius of 5″. *Top panel*: MOS1; *center panel*: MOS2; *bottom panel*: pn; *left* with SAS v6.0, *right* with SAS v5.4. Differences between SAS v5.4 and SAS v6.0 are small, and within the expected range

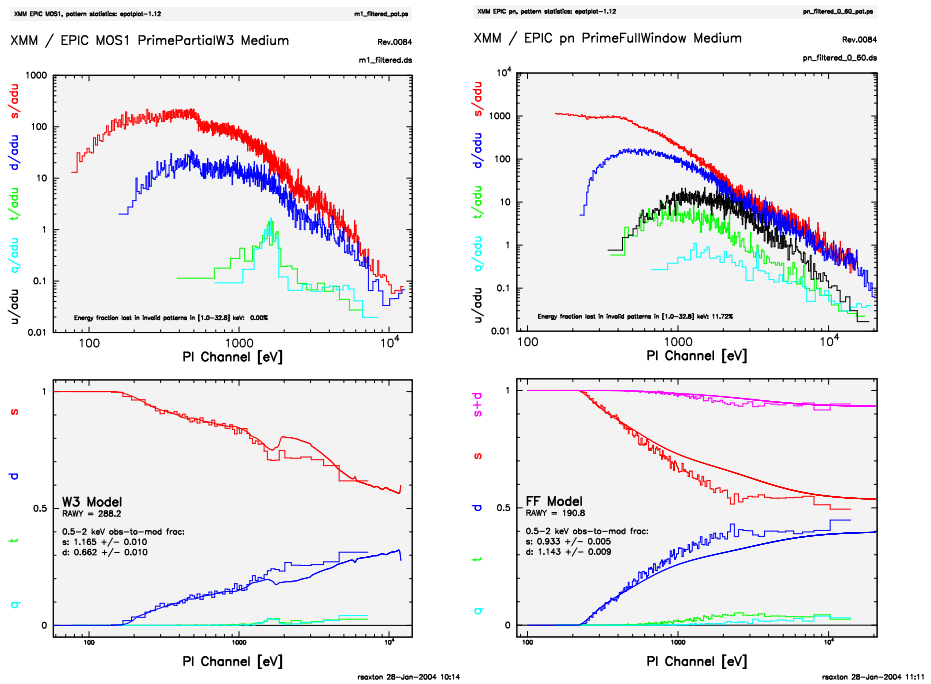

Figure 7: The `epatplot` output for circular extraction regions about PKS0558-504 for MOS-1 (`left`) and pn (`right`) in Rev.#84 (*i.e.*, before excising of the PSF core)

5.2 EPIC cameras effective area

5.2.1 PKS0558-504, Obs.#0125110101, Rev.#84

Here we analyze the first exposure of the revolution 84 observation of PKS0558-504 made with the pn detector in Full Frame mode and the two MOS cameras in Large Window mode. All of the cameras use the medium filter and suffer from a modest amount of pile-up (the count-rate is 6.5 s^{-1} for pn, and 2.7 s^{-1} for the MOS cameras).
Spectra were initially extracted from circular regions centered on the source using `especget` and were tested for pile-up using `epatplot`. All of the plots show significant deviation from the expected pattern fraction curves (Fig. 7) and it was necessary to exclude the inner $5''$ and $10''$ from the MOS and pn extraction regions, respectively to get good agreement with the model[2]. The pn data were screened for high flaring background, resulting in an exposure time of 4.7ks. These time intervals were used to extract events for all the three cameras to ensure that source variability would not affect the comparison of the camera spectra. Spectra were extracted from annuli of 5–60 (MOS) and 10–60 (pn) arc-seconds about the source with the pn time windows and standard selections of (`FLAG==0 && PATTERN<=4`) (pn) and (`FLAG==0 && PATTERN<=12`) (MOS) applied. Background spectra were extracted from source-free areas of sky near to the target and response matrices were created using `arfgen` and `rmfgen` in the standard manner. The source spectra were grouped to give a minimum number of 20 counts per channel and were fit independently with a model of a power-law and two black-bodies attenuated by absorption in cold gas fixed at the measured galactic value of $4.4 \times 10^{20} \mathrm{cm}^{-2}$. The hotter black-

[2]Users may refer to XMM-NEWS#31 (`http://xmm.vilspa.esa.es/external/xmm_news/news_list/xmm_news-2003-03-27.shtml`) for a discussion on this analysis approach

Instrument	Γ	kT^1_{BB} (eV)	N^1_{BB} 10^{-3}	kT^2_{BB} (eV)	N^2_{BB} 10^{-4}	F (0.2–2 keV) (10^{-11} erg cm^{-2} s^{-1})	F (2–10 keV)	χ^2/dof
pn	2.13 ± 0.08	79 ± 5	2.2 ± 0.2	150	8.9 ± 2.1	1.86	0.77	381/406
MOS-1	2.11 ± 0.09	69 ± 6	3.4 ± 0.5	150	8.2 ± 2.2	2.08	0.91	158/171
MOS-2	2.10 ± 0.09	73 ± 5	3.1 ± 0.5	150	8.4 ± 2.2	2.11	0.94	156/171

Table 2: Rev.#84 PKS0558-504 best-fit parameters for a power-law plus two black-body model with the hotter black-body having a fixed temperature of 150 eV. kT and N_{BB} are the temperature and normalization of the black-body components. F is the measured flux.

body temperature was poorly constrained and so was fixed at 150 eV in the fits. The best-fit parameters are given in Table 2. The fits for the two MOS cameras are seen to be in good agreement while the measured pn flux appears to be $\sim$ 10% lower than the MOS flux at low energies and $\sim$ 20% lower in the 2–10 keV band. The power-law slope of all three cameras is consistent but the pn needs a slightly higher temperature than the MOS cameras for the softer black-body component.
The best fits and residuals are presented for the three cameras in Fig. 8.

5.2.2 PKS0558-504, Obs.#0129360201, Rev.#153

Here we analyze the EPIC observations obtained in revolution 153: a pn exposure was performed in Small Window mode and MOS1 and MOS2 in Large Window mode with the Thin1 filter in place for all these exposures. The ODF was processed with the `epproc` and `emproc` tasks to generate MOS and pn calibrated event lists.
The exposures were free of flaring background and the total 10.7 ks (pn) and 7.9 ks (MOS) could be taken into account.
According to the `epatplot` created pattern statistics (Fig. 9), the EPIC window mode observations are not significantly affected by pile-up. This holds especially true for the pn Small Window exposure whereas there might be some marginal deviations of the MOS data from the model. The pn Full Frame mode exposures also taken in revolution 153 are strongly affected by pile-up, and therefore were excluded from this report.
Checking the light curves of PKS0558-504 obtained during the EPIC partial window observations (Fig. 10), the source was found to be variable. The further analysis of the spectra obtained with the three different EPIC cameras therefore was restricted to the time interval in which all instruments were simultaneously collecting data. This reduced the effective exposure time to 7.1 ks. We used `xmmselect` to display the EPIC data in sky coordinates and to define source and background regions for `especget`: Source spectra have been extracted from circular areas centered on PKS0558-504 and background spectra from source-free rectangular regions from the same CCD. Standard quality flag and pattern selections, as defined in `especget`, have been adopted: `((FLAG==0) && (PATTERN<=4))` (pn) and `((FLAG & 0x766ba000) == 0) && (PATTERN<=12))` (MOS). Response matrices have been generated on the fly by *especget* calling *rmfgen* and *arfgen*, with `detmaptype=psf`.
Source spectra have finally been grouped with a minimum number of 25 counts per channel and a factor of three by which to oversample the EPIC energy resolution.
The pn, MOS1 and MOS2 spectra have been fit individually with a model constituted of a power-law and two blackbody components all affected by foreground absorption fixed at the Galactic value of 4.4×10^{20} cm^{-2} (*baseline model*; the third blackbody envisaged by O'Brien et

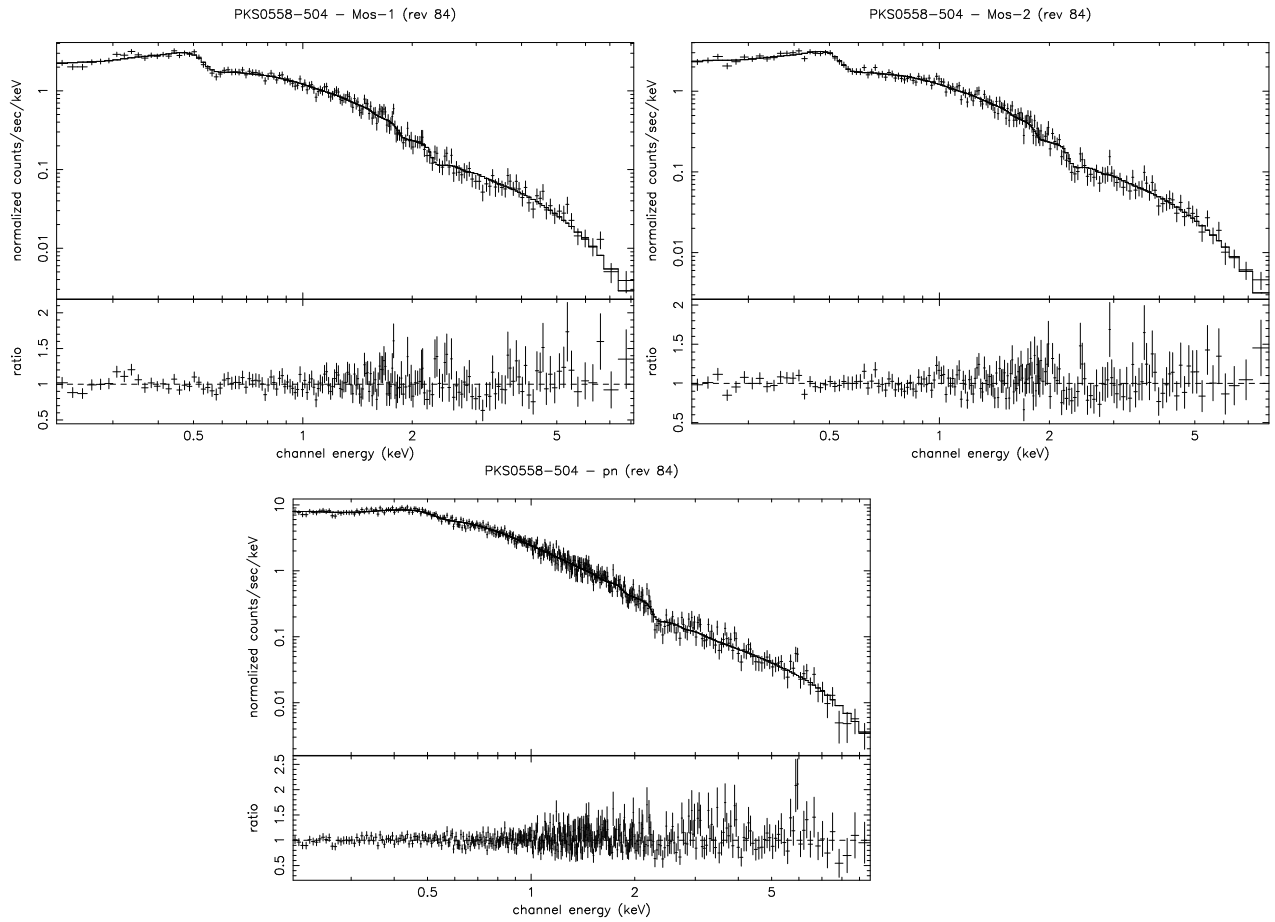

Figure 8: Spectra and residuals for MOS1 (`upper`), MOS2 (`middle`) and pn (`lower`) fits to the Rev.#84 observation of PKS0558-504 (after excision of the PSF core)

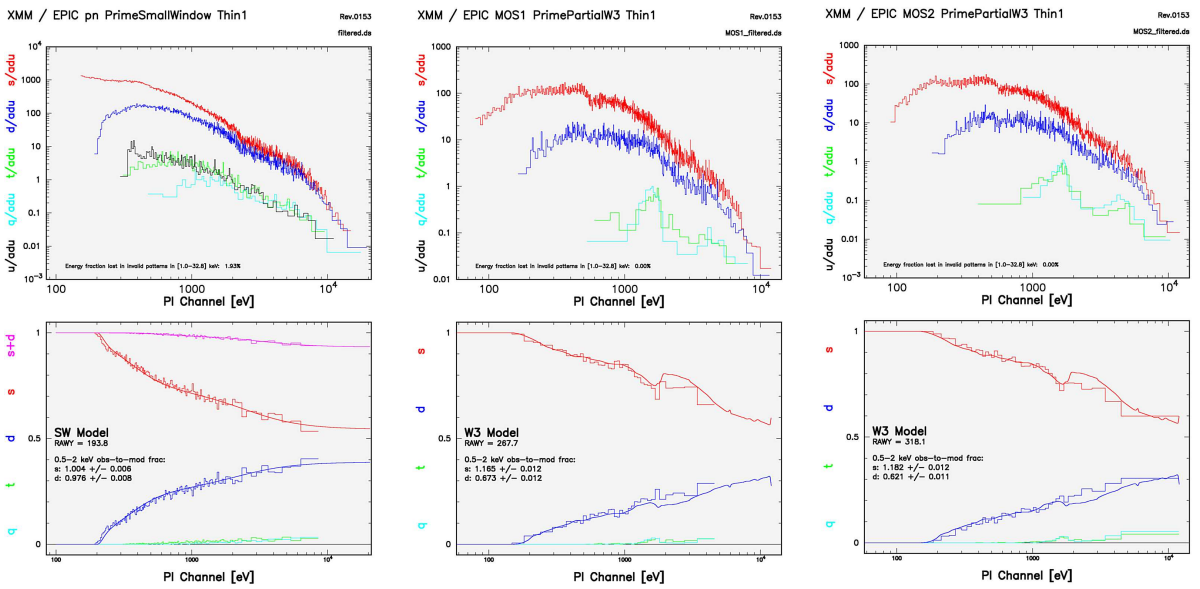

Figure 9: PKS0558-504 pattern statistics of the pn Small Window (*left panel*), and the MOS1 and MOS2 Large Window (*middle & right panel*) exposures in Rev.#153, produced by the SAS task `epatplot`.

Table 3: PKS0558-504 best-fit parameters for pn Small Window mode and MOS Large Window mode observations in Rev.#153. N are the normalizations and kT the temperatures of the blackbody components. F is the measured model flux.

	Γ	N_Γ (10^{-4})	kT^1_{BB} (eV)	N^1_{BB} (10^{-5})	kT^2_{BB} (eV)	N^2_{BB} (10^{-6})	F(0.15-2 keV) (10^{-11} erg cm^{-2} s^{-1})	F(2-10 keV)	χ^2/ dof
pn	$2.14\pm^{0.02}_{0.05}$	58 ± 3	$76\pm^{4}_{3}$	$30\pm^{2}_{3}$	$162\pm^{8}_{12}$	$116\pm^{16}_{15}$	2.73	1.20	237/203
MOS1	$2.19\pm^{0.06}_{0.08}$	$59\pm^{4}_{5}$	$67\pm^{4}_{6}$	27 ± 4	$149\pm^{15}_{16}$	$91\pm^{21}_{17}$	2.43	1.15	171/168
MOS2	$2.24\pm^{0.07}_{0.06}$	$65\pm^{4}_{3}$	$63\pm^{9}_{17}$	$21\pm^{5}_{6}$	$129\pm^{16}_{18}$	$110\pm^{47}_{15}$	2.50	1.18	155/171

al. (2001) is actually not required by the fit of this dataset).
The power-law component dominates above 2 keV, the blackbodies account for the bulk of the prominent soft X-ray excess. The spectra and best-fit models are shown in Fig. 11, together with the data/model ratio residuals. Best-fit parameters and results are summarized in Tab. 3. The fits for the individual EPIC cameras (pn, MOS1 and MOS2) agree well (cf. Table 3). We note that the fit parameters to the MOS2 spectrum show somewhat larger errors than the ones for the pn and MOS1.
We found flux differences between pn and MOS are of the order of 8-11% in the soft energy range 0.15 - 2 keV (where systematic fit residuals are found - cf. Fig. 12), whereas fluxes agree to better than 5% in the energy band 2 - 10 keV.
In addition to the camera specific fits, a simultaneous fit of pn, MOS1 and MOS2 Rev.#153 data using the baseline model was performed between 0.15 and 10 keV (see the left panel of Fig. 12). A constant factor was introduced to account for absolute flux discrepancies between the individual EPIC cameras: the factor was fixed to 100% for pn and let a free parameter for the two MOS. The residuals (cf. the right panel of Fig. 12) show that a general good agreement between the

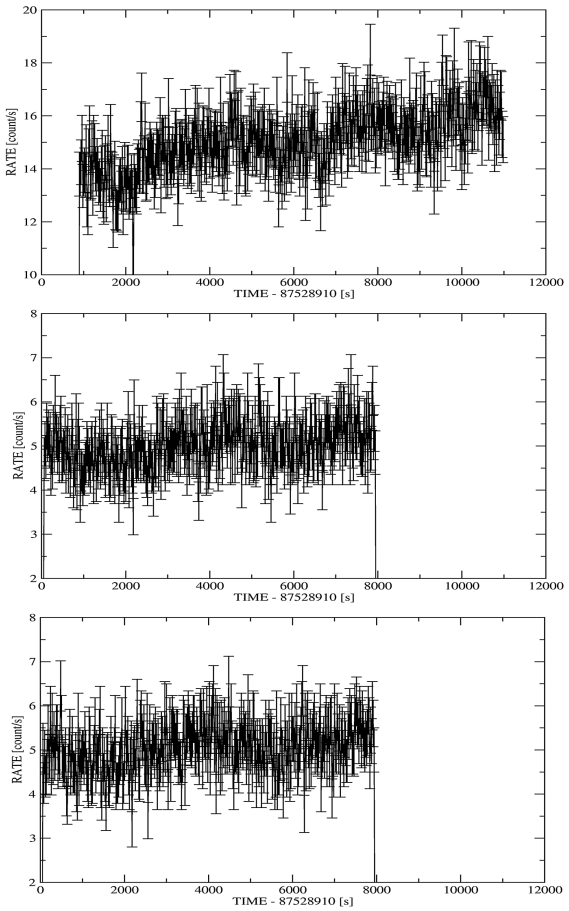

Figure 10: PKS0558-504 light curves of the pn Small Window (*upper panel*), and the MOS1 and MOS2 Large Window (*middle & lower panel*) exposures in Rev.#153. The bin-size is 20 s and the energy selection 0.15-10 keV.

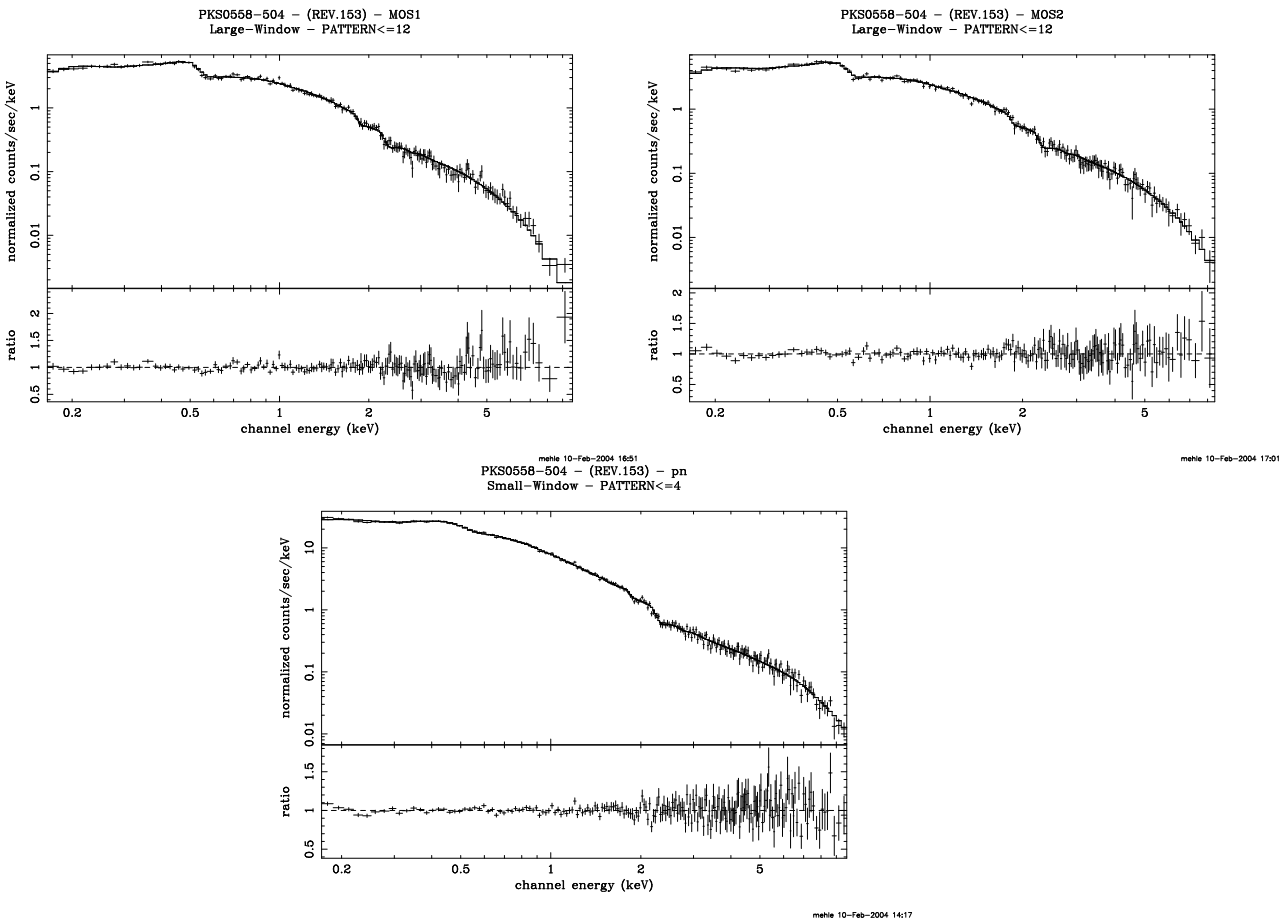

Figure 11: PKS0558-504 MOS1 (*top left*), MOS2 (*top right*) and pn (*bottom*) spectra (*upper panel*) and residuals in units of data/model ratio (*lower panel*) when the baseline model is applied to the spectrum of the Large Window exposure in Rev.#.153.

Table 4: PKS0558-504 best-fit parameters of simultaneous pn, MOS1 and MOS2 data fitting. N are the normalizations and kT the temperatures of the blackbody components. $factor$ marks the fit constants and F the model fluxes for pn, MOS1 and MOS2, respectively. The constants were introduced to allow for absolute flux discrepancies between the EPIC cameras. The pn constant was fixed to 100%. Calibrated event lists were produced by the `epproc` and `emproc` meta-tasks.

Γ	N_Γ (10^{-4})	kT^1_{BB} (eV)	N^1_{BB} (10^{-5})	kT^2_{BB} (eV)	N^2_{BB} (10^{-6})	$factor$ (%)	F(0.15-2 keV) (10^{-11} erg cm^{-2} s^{-1})	F(2-10 keV)	χ^2/ dof
2.19 ± 0.03	64 ± 2	70 ± 4	28 ± 2	149^{+5}_{-9}	116^{+14}_{-9}	100/89/92	2.74/2.43/2.51	1.24/1.10/1.13	667/542

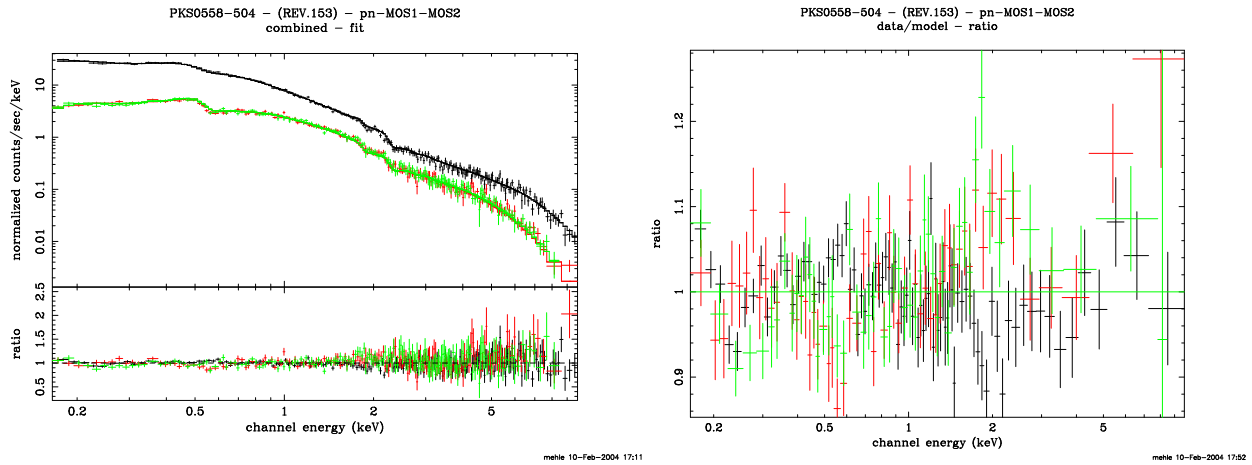

Figure 12: *Left panel*: PKS0558-504 pn (black), MOS1 (red) and MOS2 (green) spectra together with residuals in units of data/model ratio (*lower panel*) when the baseline model with additional factors for the three cameras is simultaneously applied to the spectra of the Small Window (pn) and Large Window (MOS) exposures of Rev.#153. *Right panel*: PKS0558-504 pn (black), MOS1 (red) and MOS2 (green) combined fit residuals in units of data/model ratio. Data were rebinned for clarity and plotting purposes.

cameras is achieved: the discrepancy in the cross calibration of the EPIC instruments for these modes and filter are less than 10% in the ratio data/model. The discrepancies are somewhat larger around the 1.8 keV Si-edge. For completion the best fit parameters obtained are given in Tab. 4.
The same spectral analysis as described above for the `epproc` and `emproc` generated event lists was performed also for the event lists that were produced by the pipeline processing at the Survey Science Center (SSC) with SAS `xmmsas_20040218_1831-6.0.0-Beta`. Results of the simultaneous fit of pn, MOS1 and MOS2 Rev.#153 data using the baseline model between 0.15 and 10 keV are given in Tab. 5. Both simultaneous fits (Table 4 and 5) agree within the errors.

5.2.3 G21.5-0.9

The X-ray spectrum of the Crab-like Supernova Remnant (SNR) G21.5-0.9 (Warwick et al. 2001) is well described by a strongly absorbed (column density, $N_H \sim 2 \times 10^{22}$ cm^{-2}) power-

Γ	N_Γ (10^{-4})	kT^1_{BB} (eV)	N^1_{BB} (10^{-5})	kT^2_{BB} (eV)	N^2_{BB} (10^{-6})	$factor$ (%)	F(0.15-2 keV) (10^{-11} erg cm^{-2} s^{-1})	F(2-10 keV)	χ^2/ dof
$2.20\pm^{0.04}_{0.03}$	$65\pm^{2}_{1}$	$67\pm^{2}_{4}$	29 ± 2	144 ± 8	$125\pm^{14}_{20}$	100/90/94	2.78/2.51/2.60	1.24/1.12/1.16	681/547

Table 5: PKS0558-504 best-fit parameters of simultaneous pn, MOS1 and MOS2 data (further details are given in the caption of Table 4). Calibrated event lists were produced by the SSC pipeline.

Table 6: Best-fit parameters and results when a photoelectrically absorbed power-law model is applied to the EPIC spectra of G21.5-0.9 for spectra extraction regions of 2.7' (*left*) and 1' (*right*), respectively, and `detmap=dataset`

	Extraction radius = 2.7'			Extraction radius = 1'		
Camera	N_H (10^{22} cm^{-2})	Γ	2-10 keV flux (10^{-11} cgs)	N_H (10^{22} cm^{-2})	Γ	2-10 keV flux (10^{-11} cgs)
MOS 1	2.18 ± 0.04	$1.87\pm^{0.03}_{0.02}$	6.36 ± 0.05	2.30 ± 0.04	$1.85\pm^{0.02}_{0.03}$	5.56 ± 0.05
MOS 2	2.17 ± 0.04	$1.93\pm^{0.02}_{0.03}$	6.20 ± 0.05	2.28 ± 0.04	1.89 ± 0.02	5.43 ± 0.05
pn	2.16 ± 0.03	$1.876\pm^{0.015}_{0.016}$	6.25 ± 0.03	2.24 ± 0.03	$1.838\pm^{0.015}_{0.016}$	5.32 ± 0.03

law. At 0-th order, it can be characterized through 3 quantities only: N_H, the photon index Γ and the model normalization or flux. This source is therefore particularly well-suited to compare the performance of the response matrices above 1 keV.

The XMM-Newton observation discussed in this report was performed on April 7, 2000. The EPIC cameras were operating in Full Frame (MOS), and Extended Full Frame (pn) mode, respectively. The source was on-axis. Source spectra were extracted from circular regions of 2.7' radius around the centroid of the SNR. Background spectra have been extracted from an annulus of 3.15' to 4.6' radius. The source spectra were rebinned in order to have at least 50 counts in each spectral bin and to oversample the instrumental energy resolution by a factor not higher than 3. The spectra were fit in the 0.3-12 keV and 0.1-15 keV energy bands for MOS and p-n, respectively. Effective areas were generated after generating exposure-specific detector maps, a recommended for extended sources.

The best-fit results are shown in Tab. 6 and Fig. 13, and Fig. 14. Residuals are within $\pm 5\%$ across the whole sensitive bandpass of the EPIC cameras. A difference in the spectral shape by about $|\Delta\Gamma \leq 0.07|$ is present between the MOS cameras. Otherwise, the best-fit parameters are basically consistent within the statistical uncertainties.

We stress that *wrong* results can be generated by `arfgen`, if a *flat* detector map is employed, even for an on-axis, moderately extended source such as G21.5-0.9. In Tab. 7 we report the best-fit parameters and results of the same fit as in Tab. 6, when effective areas are generated with the `arfgen` parameter `detmap=flat`. The discrepancy in normalization among the EPIC camera is much larger, and the pn measured flux becomes larger than the MOS ones for the extraction radius encompassing the whole extension of G21.5-0.9. These large differences are due to the vignetting correction, which even for sources nominally on-axis can largely differ among the EPIC cameras due to the $\simeq$1' shift between the nominal boresight position and the optical axis in the MOS 2 and pn cameras.

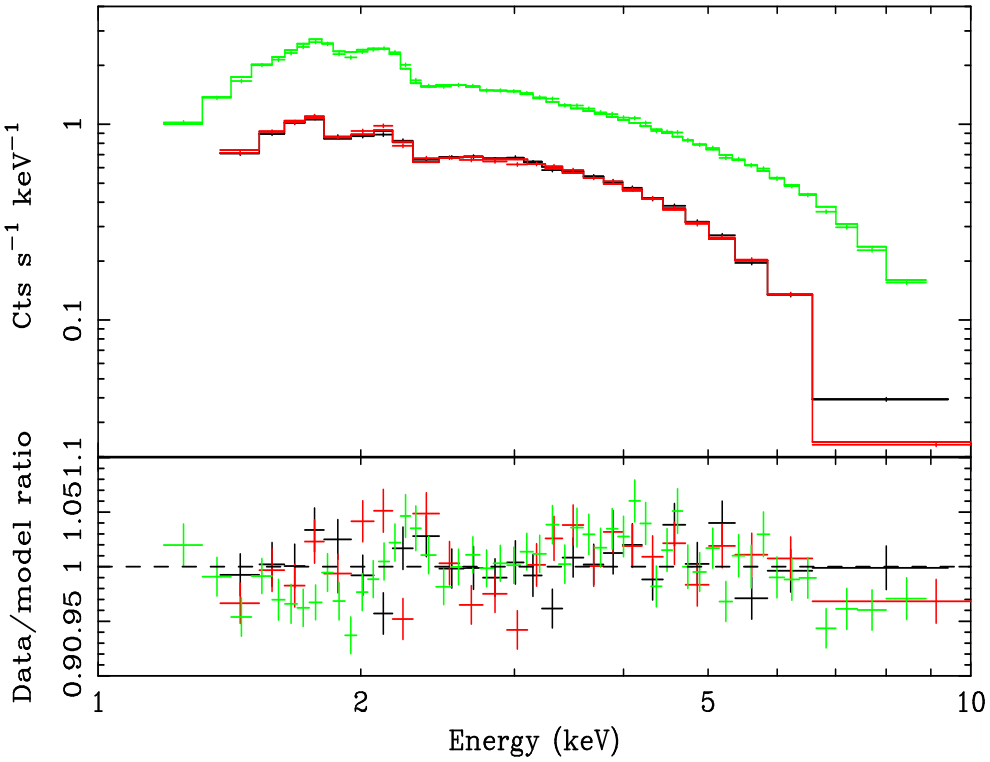

Figure 13: EPIC spectra (*upper panel*) and residuals in units of data/model ratio (*lower panel*), for the spectral fit in Tab. 6 (with extraction radius of 2.7'; MOS1: *black*; MOS 2: *red*; pn *green*). Each data point corresponds to a signal-to-noise ratio ≥50.

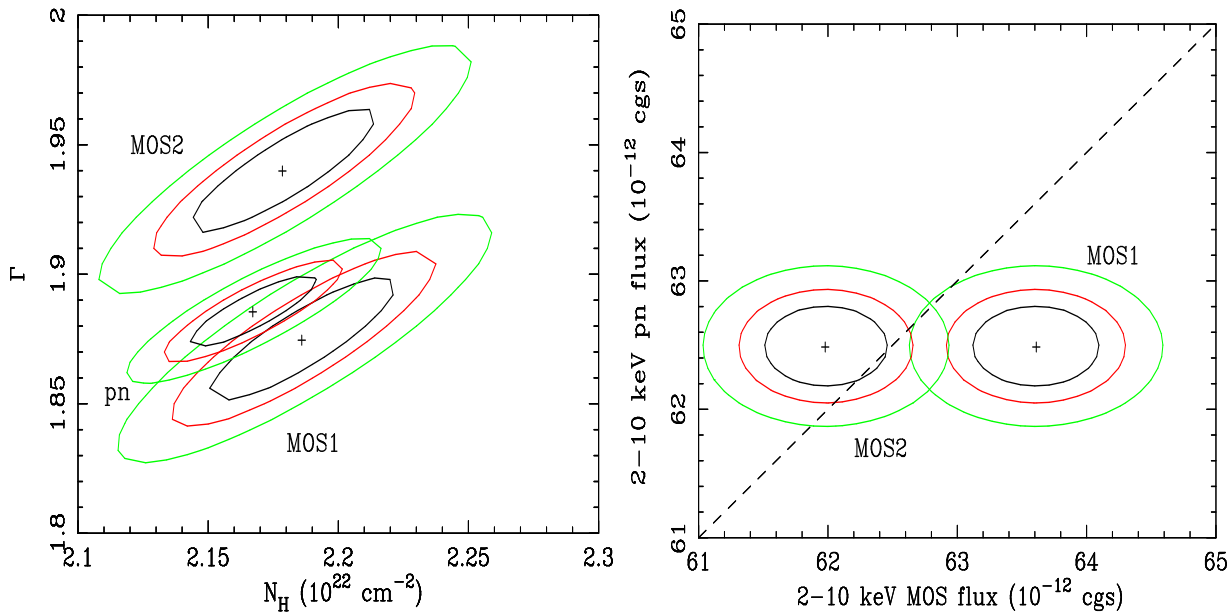

Figure 14: *Left panel*: iso-χ^2 contour plots for N_H versus Γ. Contours are at 68%, 90%, and 99% confidence levels for two interesting parameters. *Right panel*: iso-χ^2 contour plots for the MOS 2–10 keV observed flux versus the pn flux in the same energy band. The *dashed line* indicates the locus of equal fluxes

Table 7: Best-fit parameters and results when a photoelectrically absorbed power-law model is applied to the EPIC spectra of G21.5-0.9 for spectra extraction regions of 2.7' (*left*) and 1' (*right*), respectively, and `detmap=flat`

	Extraction radius = 2.7'			Extraction radius = 1'		
Camera	N_H (10^{22} cm^{-2})	Γ	2-10 keV flux (10^{-11} cgs)	N_H (10^{22} cm^{-2})	Γ	2-10 keV flux (10^{-11} cgs)
MOS 1	2.19 ± 0.04	$1.88\pm^{0.02}_{0.03}$	6.86 ± 0.06	2.30 ± 0.04	1.85 ± 0.03	6.00 ± 0.05
MOS 2	2.18 ± 0.04	1.94 ± 0.03	$6.76\pm^{0.05}_{0.06}$	2.28 ± 0.04	$1.90\pm^{0.03}_{0.02}$	$5.92\pm^{0.06}_{0.05}$
pn	$2.17\pm^{0.02}_{0.03}$	1.886 ± 0.015	7.03 ± 0.04	2.24 ± 0.03	1.836 ± 0.015	5.47 ± 0.03

Table 8: Her X-1 best-fit parameters.

Instrument	Γ	T_{in}	N_{BB}	E_{line}	σ	E_{line}	σ
pn		[eV]	[10^4]	[keV]	[keV]	[keV]	[keV]
	$0.8448\ \pm^{0.0034}_{0.0043}$	$182\ \pm^{4}_{5}$	$1.52\ \pm^{0.19}_{0.15}$	$0.5^{\dagger}$	$0.005^{\dagger}$	$0.9626\ \pm^{0.008}_{0.008}$	$0.1373\ \pm^{0.004}_{0.004}$
	E_{line}	σ	E_{line}	σ	χ^2/ dof		
	[keV]	[keV]	[keV]	[keV]			
	$6.556\ \pm^{0.025}_{0.030}$	$0.3741\ \pm^{0.044}_{0.037}$	$6.438\ \pm^{0.010}_{0.034}$	$0.005^{\dagger}$	1201.0/872		

†frozen

5.2.4 Her X-1 – pn Timing mode

XMM-Newton observed Her X-1 ($\alpha_{2000} = 16^h57^m49^s.80$, $\delta_{2000} = +35°20'32''.6$) , several times. The observation used in this report took place on January 26, 2001, Rev.#207, lasting more than 9000 seconds. For this analysis only pn data have been used. We used the following extraction regions: `((RAWX,RAWY) IN box(36.5,100,25,99.5,0))`, and `((RAWX,RAWY) IN box(5,100.75,4.5,99.25,0))`, for the source and background spectra, respectively. Spectra were extracted using single and double events neglecting the events at CCD borders and events lower than 0.5 keV where data should not be used due to the high noise below 0.5 keV in EPIC-pn Timing Mode.
Spectra were fit with a model constituted by foreground absorption, power law, disk blackbody, and four Gaussian lines (two of them broad). Several residual features are known to be due to current uncertainties in the calibration.
Fig. 15 shows a plot of Her X-1 (data and model) of the best fit to the pn Timing Mode spectrum. The best-fit parameters and results are summarized in Tab. 8.

5.2.5 Crab – pn Burst mode

XMM-Newton observed the Crab pulsar ($\alpha_{2000} = 05^h34^m31^s.97$, $\delta_{2000} = +22°00'52''.1$) in Revs.#234, 411, 698 and 700 using the pn-fast modes (i.e. Timing and Burst mode). For spectral analysis only Burst mode data of the Crab are useful, since the spectra are piled-up in Timing mode. However the timing mode observations can be used for timing analysis.
We used the following extraction regions: `((RAWX,RAWY) IN box(37,71.5,3,70,0))`, `((RAWX,RAWY) IN box(4.75,71,3,70,0))`, for the source and the background, respectively.
Spectra in the energy range 0.6–10 keV were extracted for four Burst mode observations using single and double events only neglecting the events at CCD borders. The spectra were fit with

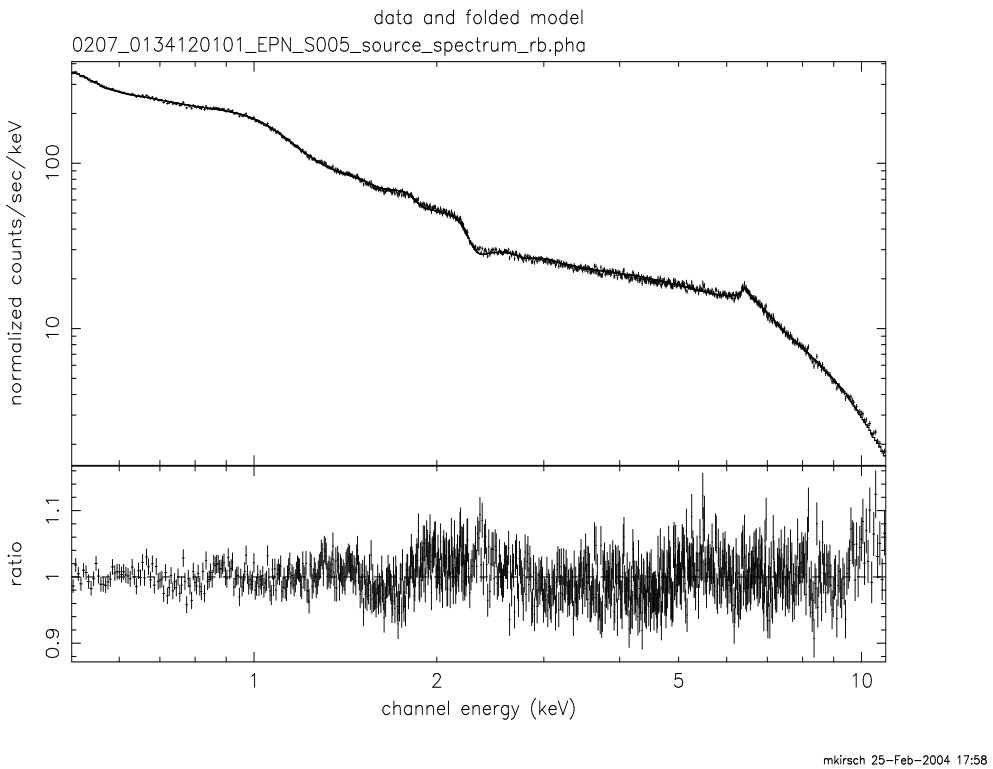

Figure 15: Spectrum of Her X-1 in EPIC pn Timing mode

Table 9: Crab best fit parameters when observed in pn Burst Mode.

Γ	$Norm$ [photons $(keV)^{-1}$ cm^{-2} s^{-1}] @ 1 keV	N_H [10^{22}]	χ^2/ dof [keV]
$2.051\pm^{0.003}_{0.003}$	$5.634\pm^{0.018}_{0.017}$	$2.61\pm^{0.01}_{0.01}$	8600/5553

a model constituted by foreground absorption, and a power law. Several residual features are known to be due to current uncertainties in the calibration.
Figure 16 shows the Crab (data and model) of the best fit to the pn burst mode spectrum. Note that the fit was performed using an overall normalization constant for each spectrum. All the normalization constants agree within 0.5%. The best-fit parameters and results are summarized in Tab. 9.

5.2.6 On the relative normalization among the EPIC cameras

Users should refrain from extrapolating general conclusions from the values of the cross-normalization among the EPIC cameras presented in this document. An improvement with respect to previous SAS Science Validation reports exists, mainly due to a new definition of the optical axis, which allows a more accurate vignetting correction. Nonetheless, values differing by $\pm 10\%$ in both the soft and the hard X-ray bands are possible, depending on the instrumental configuration and the intrinsic source spectral properties. A full characterization of this quantity will be the subject of a forthcoming paper (Kirsch et al., in preparation). Users are recommended to refer

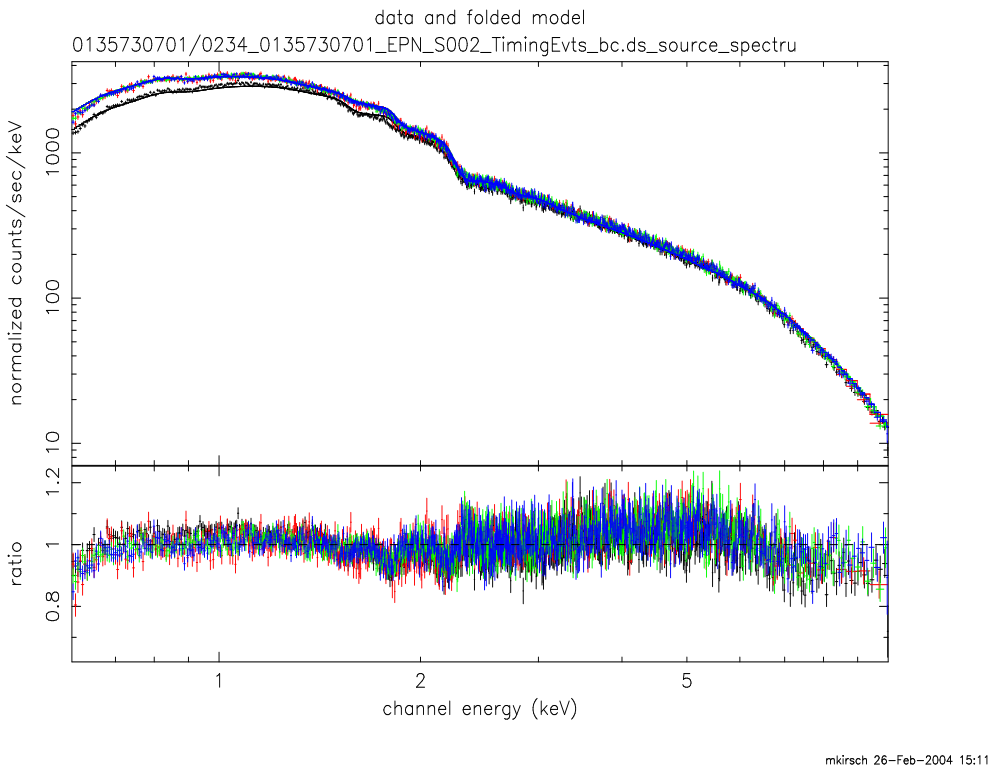

Figure 16: Spectra of the Crab in EPIC pn Burst mode

to the EPIC Calibration Status document (`http://xmm.vilspa.esa.es/docs/documents/CAL-TN-0018-2-1.pdf`) for updates on this matter.

5.3 EPIC cameras timing

The EPIC-pn event analyzer (EPEA) uses the CDMU 1 Hz clock pulse to increment an internal 15 bit wide counter (FTCOARSE) and to reset a 16 bit sub-second (FTFINE) counter which is clocked with 48828.125 Hz. Thus the pn CCD data frames are time stamped with a resolution of 20.48 ms by FTCOARSE/FTFINE pairs. In an ODF they form two columns in the first table of the pn Auxiliary Data File (AUX) which are accessed by SAS in the process of converting frame counters to absolute photon arrival times.
In mid-2000 it was first discovered that the pn AUX data exhibit certain kinds of anomalies whose frequency of occurrence is variable and apparently unrelated to camera mode, observing time or duration. Obviously all these problems need to be corrected for, as otherwise the event times turn out wrong. This is especially critical, as a single shift in FTCOARSE time will cause all subsequent times to be wrongly shifted by the same amount. Pulse profile analysis with a data set that contains a single or multiple undetected and uncorrected such time jumps will then be inconclusive because all photons after the instant of the time jump will be out-of-phase. This can result in a pulse peak broadening, phase shift or the appearance of spurious pulse components. As examples Figure 17 show the significant influence of time jumps on χ^2-distributions of epoch folding period search. Absolute timing analysis was likely impossible for obvious reasons. In the past these anomalies have all been seen and led to difficulties in the interpretation of obtained

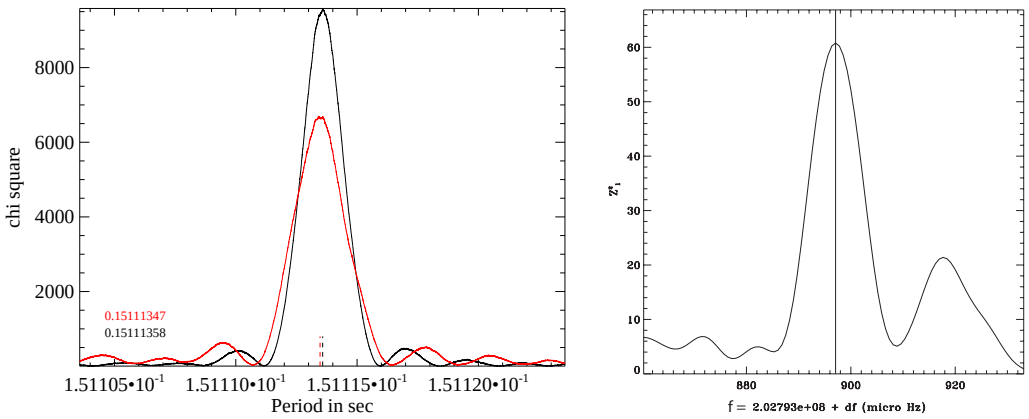

Figure 17: Left: Influence of a time jump of 31 s on the χ^2-distribution of epoch folding period search (pulsar period 150 ms). Red: time jump not detected. Black: time jump detected and corrected. The time jump causes broadening of the χ^2-distribution and increases the presence of secondary maxima. Right: Influence of a time jump of 1 s on the Z^2-distribution of epoch folding period search (pulsar period 4 ms). The extrapolated radio period is indicated and agrees with the period found in the XMM-Newton data within the errors. A second major maximum appears. (Kirsch et al. 2004)

results.
The SAS since the early days can reliably detect and correct for the anomalies with the exception that the detection logic for some cases sometimes seems to fail with the consequences described above. With the new SAS release we are now in a state that all problems are reliably found and corrected for the fast pn modes (Timing and Burst). There might be still some rare cases of time jumps in the imaging modes.
Figure 18 shows χ^2-epoch folding for different Crab observations, with a resolution of 1×10^{-10} s.
In the following analysis we performed χ^2-distributions of epoch folding for all Crab observations is the fast EPIC pn modes. Each observation was folded using the radio period as a start value and the epoch of the respective radio period. We determined the X-ray period by calculating the weighted mean of the periods in each epoch folding using all periods for χ^2 values greater than 50 % of the maximum χ^2. We give in Fig. 19 the characteristic value for relative accuracy of timing analysis $\Delta P/P$ where $\Delta P = P_{radio} - P_{xray}$ and $P = P_{radio}$. The relative timing of XMM-Newton is now considerably better than 10^{-8}.

5.4 MOS Timing Mode CTI correction

The MOS Timing mode CTI correction has been refined. A verification was performed on the SNR 1E0102-7219, where prominent lines have been fitted for both MOS cameras in Large Window and Timing mode. Fig. 20 shows the spectrum of the SNR, whereas Fig. 21 illustrates the results of the fits to the different lines. The MOS Timing mode energy calibration does now agree in the energy range 0.4–2.0 keV with the Large Window mode within ±0.5%.

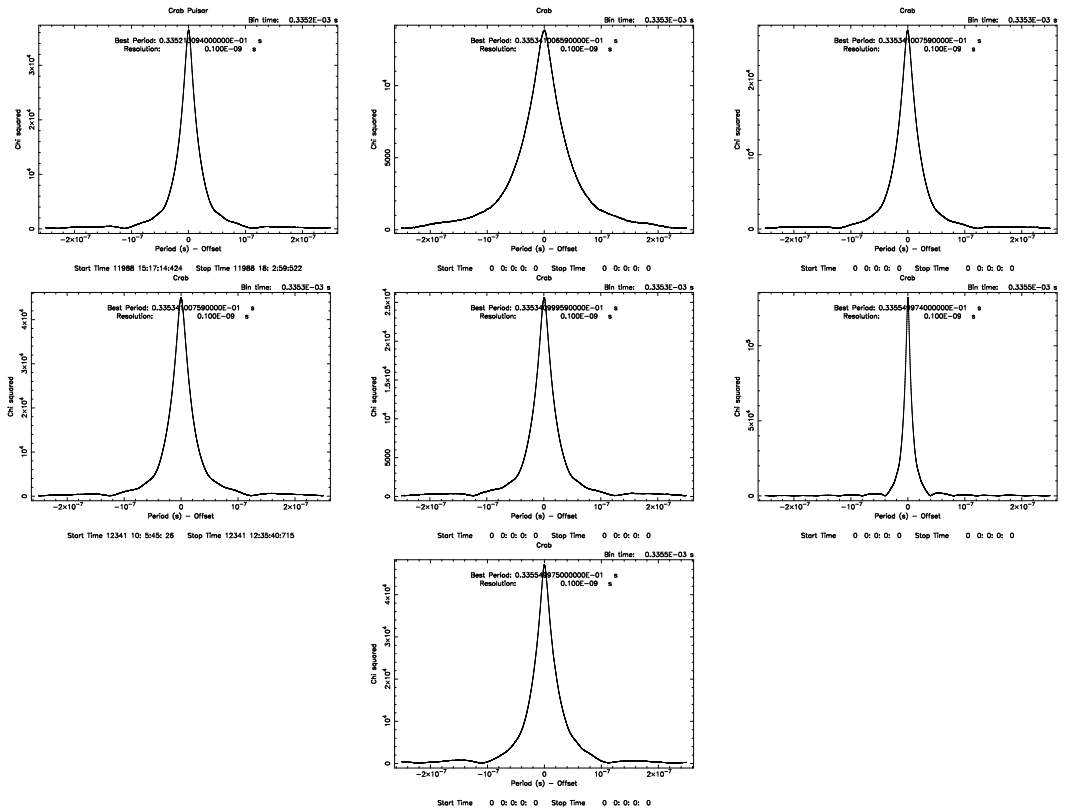

Figure 18: χ^2 epoch folding for different Crab observations. Note that all possible time jumps are corrected in the fast pn modes and the χ^2 distributions is smooth as it should be.

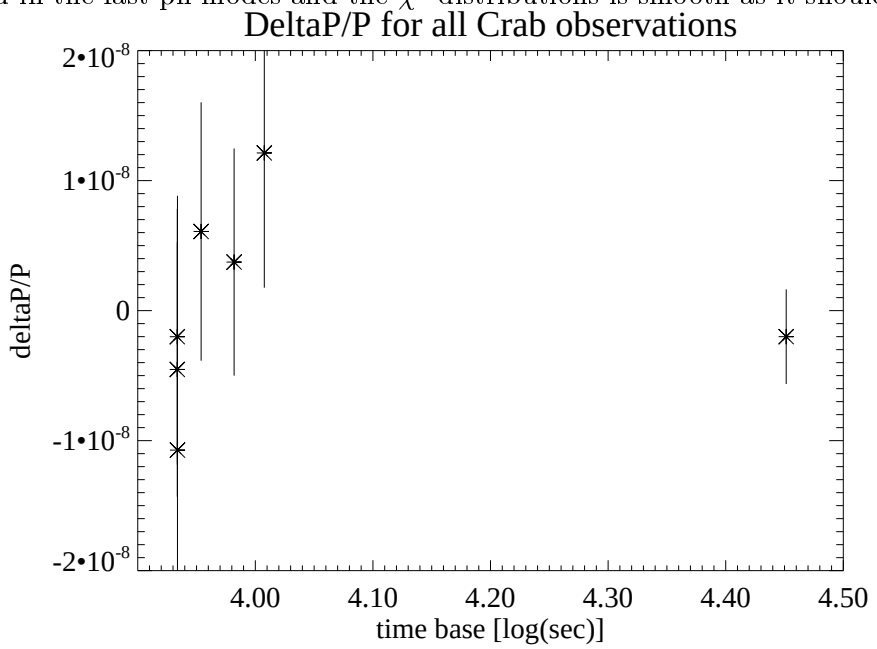

Figure 19: $\Delta P/P$ for all XMM-Newton Crab observations (EPIC-pn). On the x-axis logarithmically the total time base of the observation is plotted. Of course for longer observations the relative timing accuracy is better.

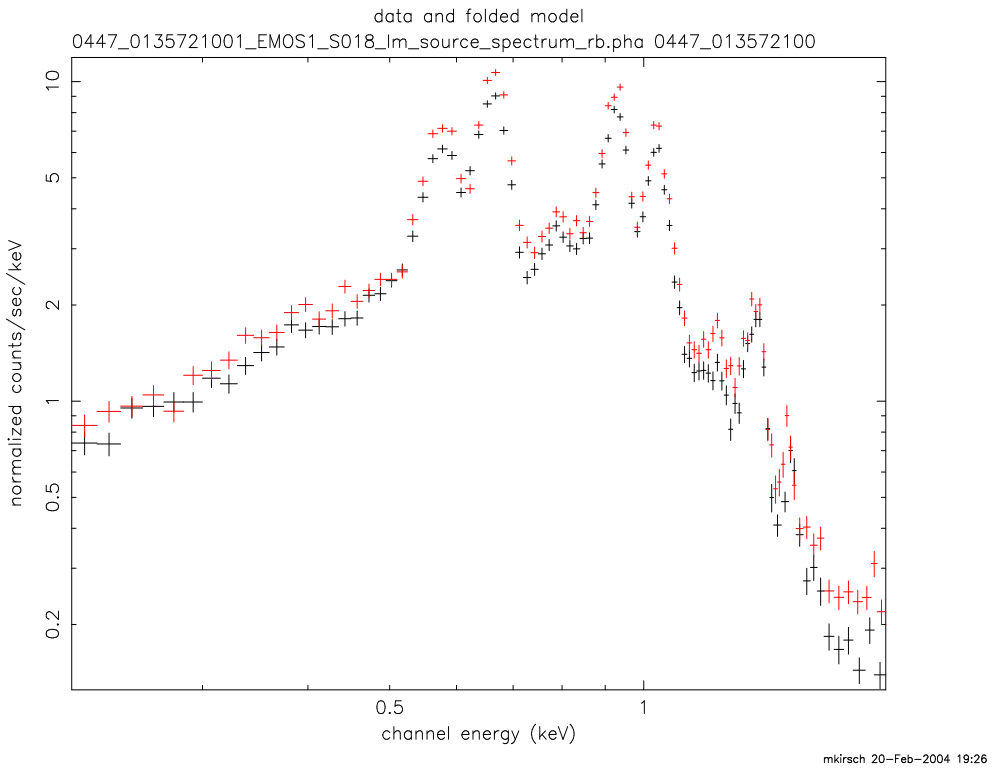

Figure 20: Spectra of the SNR 1E0102-7219 in MOS1 Large Window (black) and Timing (red) mode.

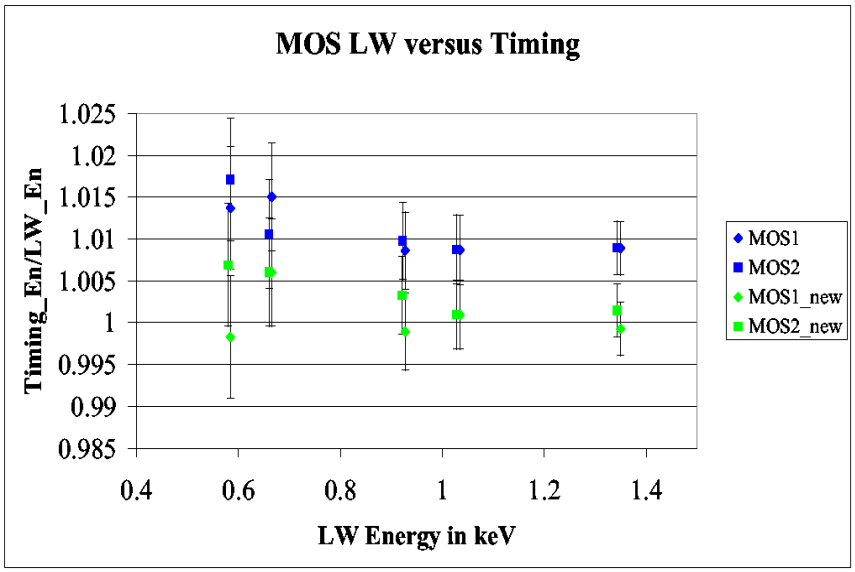

Figure 21: Line positions of the SNR 1E0102-7219 for MOS Large Window and Timing mode. Blue old CTI correction, green new CTI correction.

Table 10: The Standard Johnson UBV magnitudes of the BPM 16274 from Eggen and XMM-Newton OM.

	U	B	V
Eggen's values	13.375	14.185	14.20
derived from OM	13.358	14.195	14.201

Table 11: The OM count rates and flux densities of BPM16274

	V	B	U	UVW1	UVM2	UVW2
OM count rates	32.23	106.73	111.84	71.63	29.41	14.36
conversion factors	2.17E-16	1.04E-16	1.77E-16	4.39E-16	2.02E-15	5.79E-15
Flux densities	6.99e-15	1.11e-14	1.98e-14	3.15e-14	5.94e-14	8.31e-14

5.5 OM filter photometry

The white dwarf BPM 16274 is an OM routine calibration target, which is used for monitoring OM performance and calibration. The observation used in this report took place on May 13, 2001, Rev.#261. For U, B, V, UVW1, and UVW2 filters, the observations were carried out in Image Mode, and for UVM2 filter, the observation is in Full Frame Low Resolution mode.
The standard Johnson U, B, V magnitudes of the BPM 16274, which have been reported by Eggen, are shown in the first row of Tab. 10 The OM u,b,v instrumental magnitudes of the BPM16274 are 13.138, 14.192, 14.193, respectively. The color transformation from the OM instrumental system to Johnson's system has been established and is available through OM_COLORTRANS CCF.
In order to transform OM magnitudes into Johnson's UBV system, the following transformation equations in the CCF are used.

$$B - V = -0.0005 + 1.046 \times (b - v) - 0.023 \times (b - v)^2 \quad (1)$$

$$V - v = -0.0008 - 0.006 \times (b - v) - 0.021 \times (b - v)^2 \quad (2)$$

$$U - B = -0.002 + 0.901 \times (u - b) + 0.103 \times (u - b)^2 \quad (3)$$

The standard magnitudes derived by OM are shown in the second row of Table 1. We can see an excellent agreement between Eggen's catalog values and that derived from XMM-OM.
In order to convert the OM count rates to flux, the flux conversion factors in the current calibration file (CCF) are used. For each filter, multiplying the count rates (counts/s) from SAS OM source list files by the flux conversion factors yields the flux densities (expressed in erg/cm^2/s/A). Tab. 11 gives the OM count rates from PPS files, the flux conversion factors, and derived flux densities of BPM16274 in each filter. Fig. 22 shows BPM 16274 spectrum (dashed line) retrieved from HST standards, altogether with OM derived fluxes (red crosses). The OM flux values are within 10% of the listed HST standard fluxes.

5.6 OM astrometry

We have used the composite of the five partial images for BPM 16274 observations taken in the standard Imaging mode (thus a full FOV) to investigate the astrometric accuracy of OM.

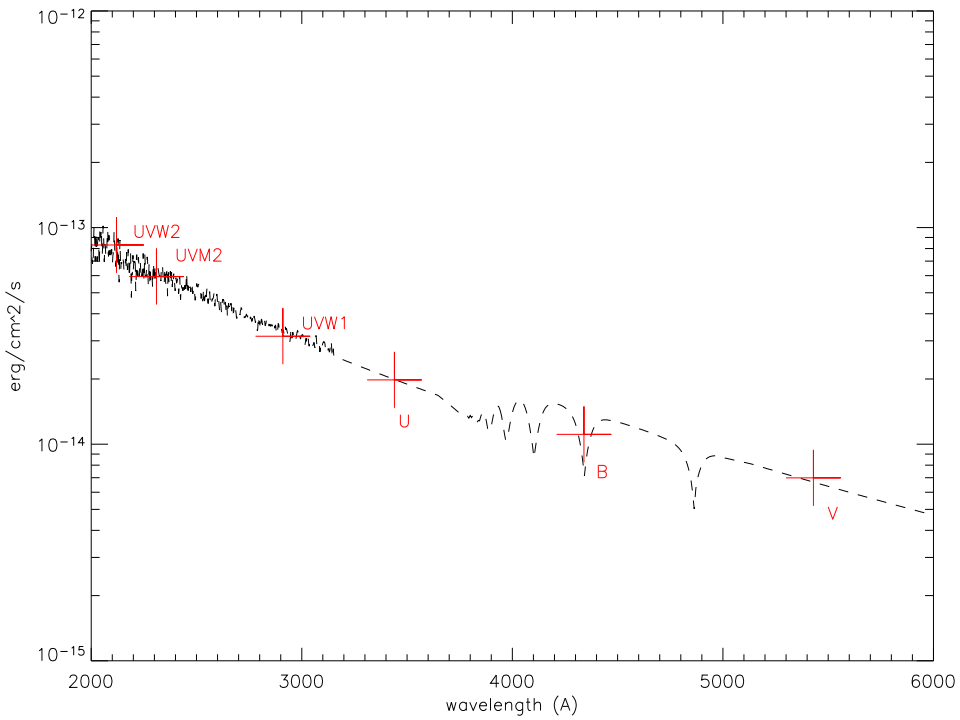

Figure 22: BPM 16274 spectrum (dashed line) retrieved from HST standards altogether with OM derived fluxes (red crosses).

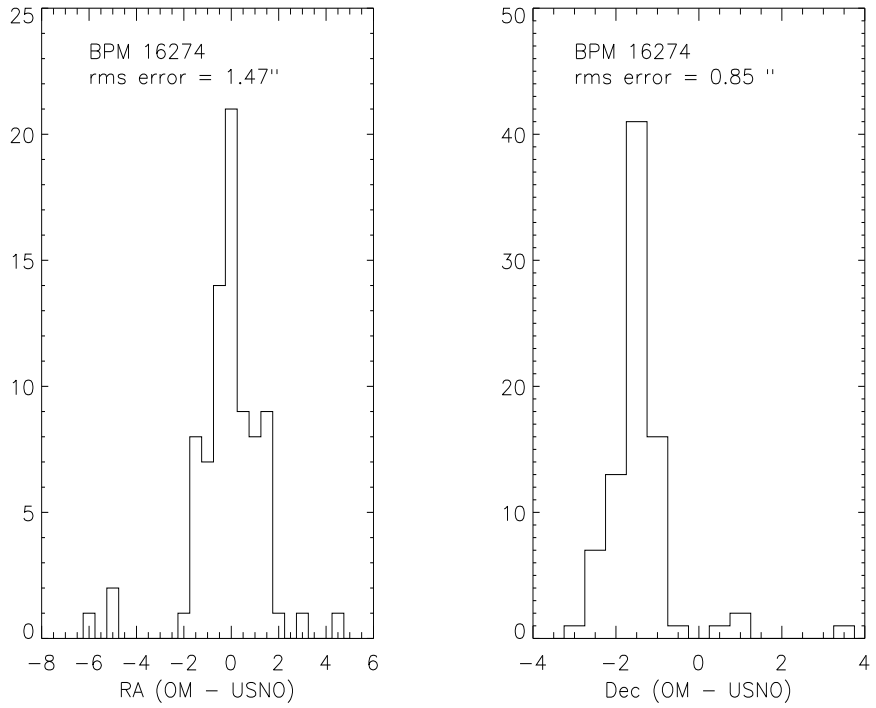

Figure 23: Histograms of the position differences for the matched pairs between OM and USNO in RA (left) and Dec (right)

The OM source list in v filter is cross correlated with the USNO A2.0 catalog. For each USNO object in the field the closest OM source within $6''$ radius is identified. Fig. 23 shows the histograms of the position differences for the matched pairs between OM and USNO in RA and Dec, respectively. This gives a r.m.s. error of $1.47''$ in RA and $0.85''$ in Dec, which is in agreement with the OM calibration status report ($\simeq 1''$).
The source positions determined by SAS are based on the satellite attitude information, and are not cross-correlated with any catalog. A few arc-seconds offset from the real position can exist due to the pointing error. For this BPM16274 observation, from Fig. 23, we found the offset is -0.09$''$ in RA and -1.42$''$ in Dec. In order to provide an estimation on the accuracy of the OM absolute astrometry, we have cross-correlated several hundreds of XMM-Newton observations with the USNO catalog. Our preliminary result shows that OM source positions have an accuracy of about 3–4$''$, before rectification with respect to an astrometric catalog. This rectification function is provided by the SAS task `omatt`, although this is not currently in the SSC pipeline.

5.7 OM grisms wavelength scale and flux calibration

The main source of error in the grism wavelength scale is due to the determination of the centroid of the zero order. The analysis of SV data as well as of other grism data, performed by the OM Team at VilSpa, shows that discrepancies of a few, 3 or 4, pixels produce shifts in the wavelength scale of up to 10 Å for the UV grism and 20 Å for the Visible one. Cases as the one presented in Fig. 2, where the detection of the zero order is perturbed by its excessive brightness or by other

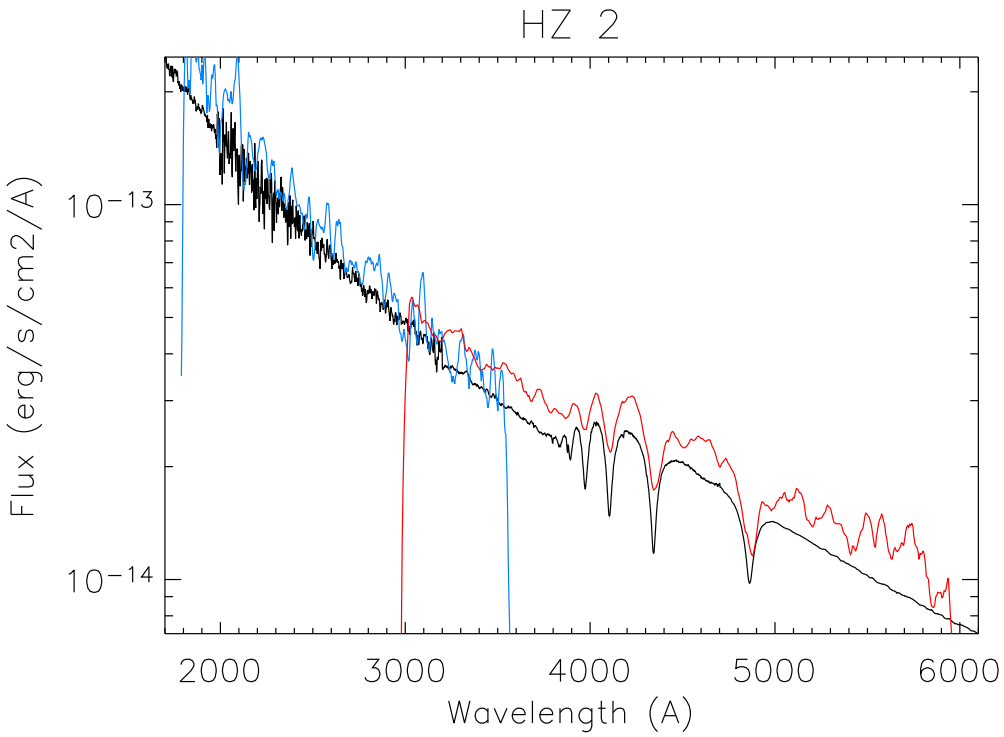

Figure 24: Flux calibrated spectrum of HZ 2. Standard flux is given in black. Blue is OM UV grism. Red is OM Visible grism.

close-by spectra or image features, can have displacements on the scale of up to 50 Å. These cases are handled much better by using the interactive task `omgsource` which allows the user to constrain the centroiding as shown in Fig. 5.
The accuracy of the wavelength scale can be appreciated in Fig. 24, where the hydrogen lines of HZ 2 in the OM Visible grism spectrum of the star appear superimposed on its standard spectrum obtained from the HST CALSPEC database.
The grisms flux calibration is based on observations of several standard stars, one of which is HZ 2. We have performed a consistency check by comparing the flux given by SAS processing for this star with its original standard flux. Fig. 24 presents such a comparison. Fluxes obtained by the SAS processing of the grisms are higher (17% for UV grism and 22% for Visible grism) than the standard flux of the star. Such a large discrepancy may be due to the fact that the values of the Inverse Sensitivity Function given by the OM_GRISMCAL CCF were obtained with data analyzed outside the SAS, using a different spectral extraction technique. A new flux calibration, based on data processed and extracted with SAS will be available in the near future. These errors should then be considerably reduced.
The consistency of the flux calibration of both grisms in the common wavelength region, between 3000 Å and 3600 Å, better than 10 %, can also be appreciated in this figure.

5.8 OM Fast Mode timing accuracy

X1822-371 is a low-mass X-ray binary which was observed with XMM-Newton on March 7, 2001, Rev.#228. The observation has been taken in XMM-OM FAST mode with UVW1 filter. The PPS files include 15 time series created by SAS `omfchain`, corresponding to 15 Fast mode

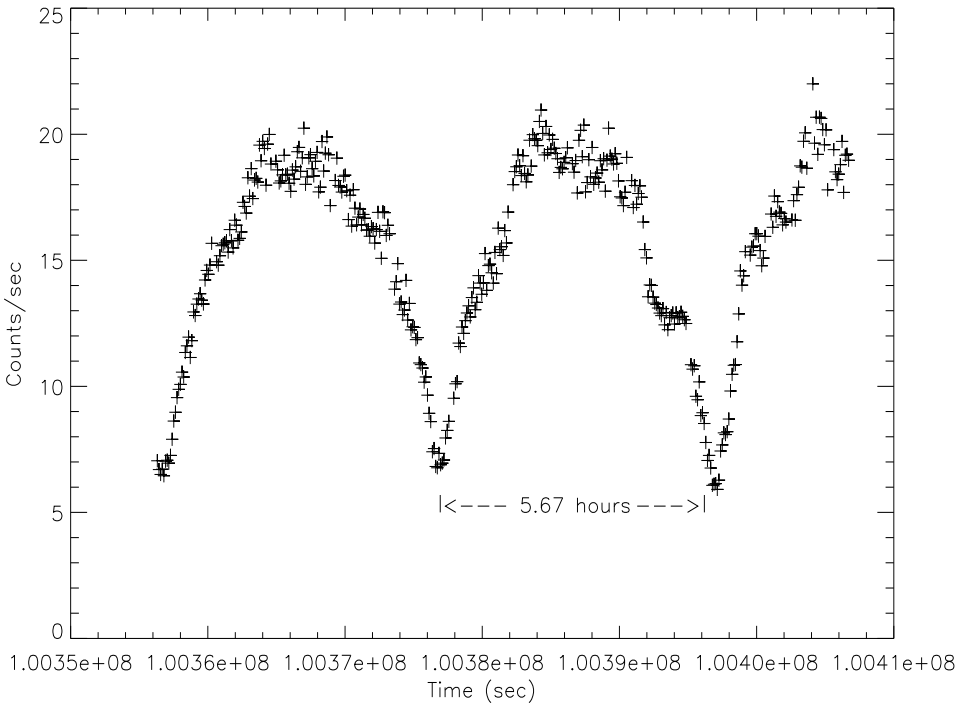

Figure 25: The OM UVW1 light curve of the low-mass X-ray binary X1822-371.

exposures. Fig. 25 shows the OM UVW1 light curve by combining all separate time series. The shape of the X1822-371 light curve is relatively repeatable from cycle to cycle, but there are inevitable small variations. The period from the OM light curve is about 5.67 hours, which is in good agreement with the period derived from the EPIC-pn light curve.

5.9 RGS effective area

The RGS effective area calibration has remained the same since the release of SAS v5.3, while the SAS tasks corresponding to the RGS data reduction have been considerably improved, mainly with respect to robustness and flexibility. In SAS v6.0 also an alternative approach for the subtraction of the CCD offset signal has been implemented, which could become the default in future versions.

We have reduced the Markarian 421 observation using `rgsproc` with all defaults without any special data selection. The observation is only very marginally affected by short periods of higher background. The results from the simultaneous fit of RGS1 and RGS2 first order background subtracted spectra with a broken power law model in the range 0.3–1.9 keV are shown in Fig. 26. There was no free normalization between the spectra, and the results show an agreement of better than 10%, over the entire region. The same qualitative answer is given by the fit to RGS1 and RGS2 both in first and second order, as shown in Fig. 27. The high energy region above 1.4 keV, however, show some larger discrepancies between first and second order, which are, however, bounded by ±20% at the highest energies.

The results of the fit are given in Tab. 12. A number of small calibration improvements are contributing to a better chi square of the total fit (1.30 per Degrees of Freedom. DoF), compared

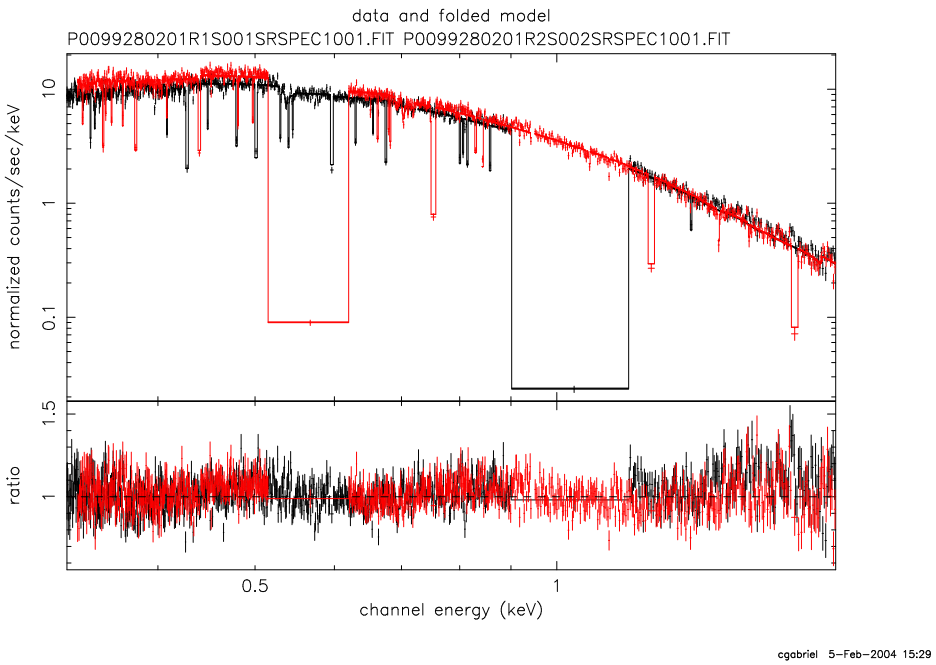

Figure 26: Mkn421 RGS1 (*black*) and RGS2 (*red*) spectra, fitted with a broken power law model

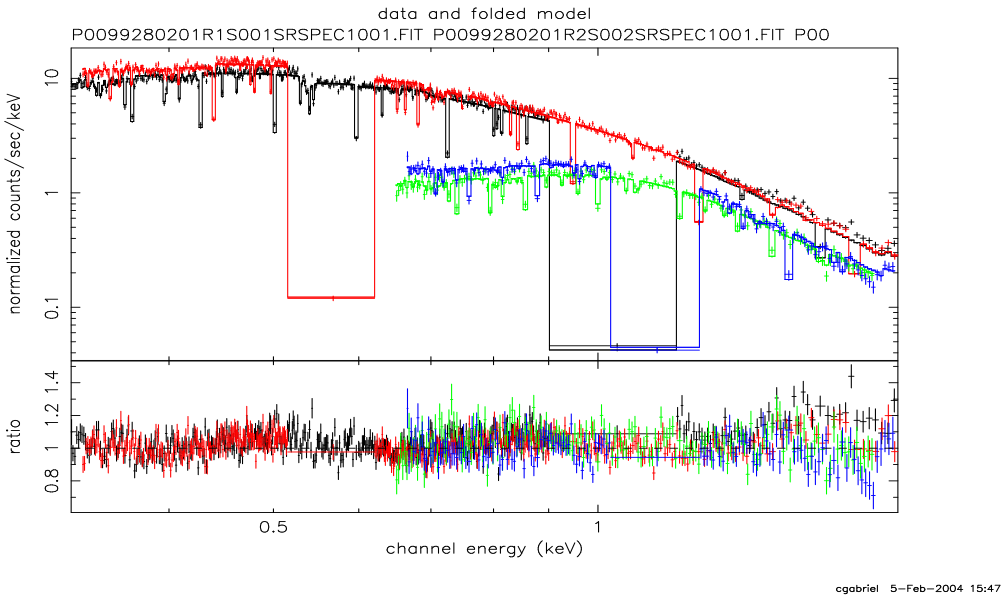

Figure 27: Mkn421 RGS1 first (black) and second (green) order spectra, RGS2 first (red) and second (blue) order spectra, fitted simultaneously with a broken power law model

Table 12: Mkn 421 best-fit parameters fitting a broken power law model to first and second order spectra of RGS1 and RGS2

Γ_1	Γ_2	$E_b(keV)$	χ^2/ dof
1.71 ± 0.02	2.45 ± 0.02	0.79 ± 0.1	11070/8519

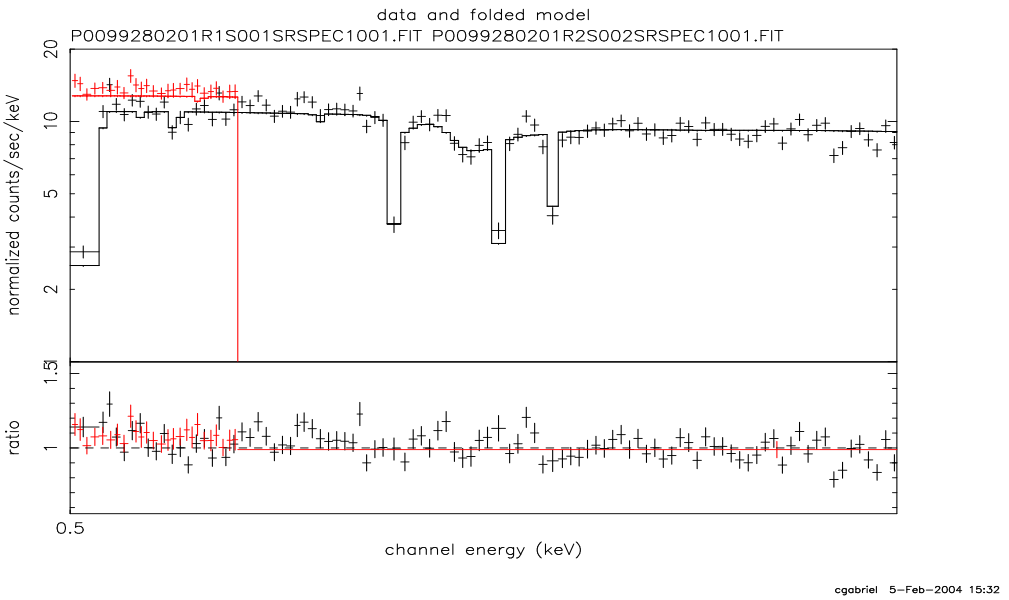

Figure 28: Mkn421 data and fit results of the area around the instrumental oxygen edge (RGS1 first order)

to that reported by the validation of SAS v5.3.x (1.47/ DoF). They include an improved model of RGS oxygen absorption, as explained in CCF release note 143 (`http://xmm.vilspa.esa.es/docs/documents/CAL-SRN-0143-1.0.ps.gz`), which is shown in the high quality of the fit in the region around the oxygen edge at 0.55 keV (Fig. 28). A large contribution to a better fit is, however, the recognition of "low count" columns as bad columns. They are now rejected by the SAS, due to an updated calibration file (cf. `http://xmm.vilspa.esa.es/docs/documents/CAL-SRN-0130-1-0.ps.gz`).

5.9.1 Pixel-by-pixel offset subtraction

One of the new implementations in SAS v6.0 is the possibility of subtracting the CCD offset signal using a new class of RGS offset files containing system offset values per CCD pixel, instead of the default value per CCD node. The new RGS offset files are derived by averaging all the diagnostic data collected within three consecutive revolutions and included in the ODF. It has been shown in an internal RGS report (`http://xmm.vilspa.esa.es/docs/documents/CAL-SRN-0146-0-1.ps.gz`) that this method can lead to a significant improvement of the data quality. However, the parameters for applying

this correction have to be optimized, and therefore the method has not (yet) become the default. The results obtained with a data reduction run using the pixel-by-pixel offset subtraction were fully compatible with the default reduction procedure, although a small reduction of the quality of the fit (1.288/ DoF instead of 1.295/ DoF) is appreciable.

5.10 RGS wavelength scale

In order to assess the accuracy of the RGS wavelength scale, we have used XSPEC v11.2.0 to analyze the spectra produced by SAS v6.0 of the four observations in the validation harness of the line-rich active star AB Dor in order to compare observed line positions with their expected laboratory values. Due to its constant XMM visibility, regular use has been made of this star for wavelength calibration purposes. It is known (Lorente et al. 2003) that the RGS wavelength scale is subject to small but significant systematic errors of a few mÅ that are not yet understood but which vary between observations and are predominantly to the red. The four observations chosen for validation were examples for which earlier SAS versions had shown to have relatively large systematic shifts.
In contrast to earlier validation exercises, we have made explicit use of the response matrices that are produced specifically for this purpose with the spectra. By necessity, these routine matrices are calculated on a relatively coarse 3400-point wavelength grid that is good enough for rough line position estimates. The statistics of RGS spectra are such, however, that line position uncertainties of 1mÅ or better are possible and more finely grained matrices are required. So, in addition, we generated 50000-point redistribution matrices between 6 and 38Å. RGS1 and RGS2 were analyzed separately, combining 1st and 2nd orders in both to enable, as far as RGS1 is concerned, the gap to be filled in left by the absence of data from CCD 7.
The entire RGS spectrum of AB Dor was modeled with an absorbed bremsstrahlung continuum and the set of lines shown with their laboratory wavelengths in Table 13. AB Dor lines are consistent in width with the instrumental response in both first and second order so they were all treated with a local delta function model. For each ion, the first line in the table was treated as a reference point against which the wavelengths of subsidiary lines were fixed by the ratios of their laboratory wavelengths. The fluxes were free except for the minor component of the Lyman doublets which were fixed at half of the principal component. We realize that this automatic procedure has some limitations but the overall fits were good and give a summary of the wavelength accuracy of the RGS1 and RGS2 instruments over their whole bandwidth. Observers should be able to get better performance from individual observations by paying special attention to the lines, blends and continuum in limited stretches of data. The results of the automatic procedure are shown in Figs. 29 and 30 which should be considered in the wider context of more extensive analysis done with SAS v5.3 (Gabriel et al. 2002).
The results of this limited validation exercise are that with SAS v6.0, the RGS is able to determine wavelengths within an accuracy of a few mÅ which amounts to better than 10% of the line widths. Fitting the distributions of Fig.30 with Gaussians yields the following parameters:

$$\begin{array}{lll} \text{RGS1} & <\Delta\lambda>=+4.5\text{mÅ} & \sigma_\lambda = 5.8\text{mÅ} \\ \text{RGS2} & <\Delta\lambda>=+7.8\text{mÅ} & \sigma_\lambda = 9.1\text{mÅ} \end{array}$$

6 XMM-Newton instrument cross-calibration

The observation of the radio-loud Narrow-line Seyfert 1 galaxy PKS0558-504 ($\alpha_{2000} = 05^h59^m47^s.00$, $\delta_{2000} = -50^\circ26'51''.0$) from Rev.#153 was used to assess the status of cross calibration for all X-ray instruments on board XMM-Newton. We used the following exposures for the different

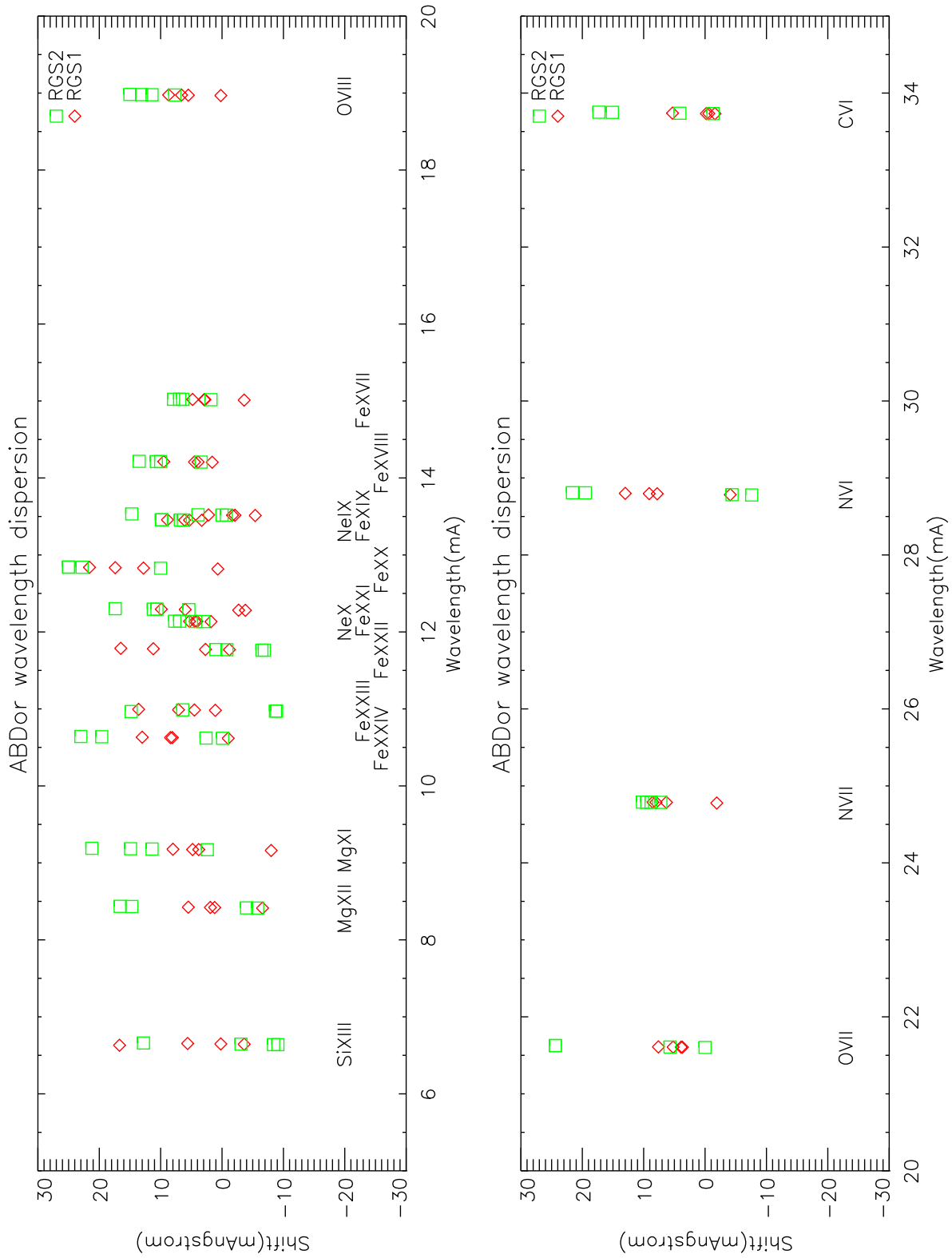

Figure 29: The wavelength shift $\Delta\lambda = \lambda_{\rm observed} - \lambda_{\rm laboratory}$ in mÅ for the 18 ions used to model the RGS spectra of 4 observations of AB Dor plotted against the laboratory wavelength of the main line of the ion concerned. RGS1 and RGS2 are shown separately.

Table 13: Laboratory wavelengths of the lines used to model the RGS spectra of AB Dor.

Ion	Laboratory Wavelength (Å)			
C VI	33.7342,33.7396	28.4652,28.4664		
N VI	28.7871	29.0840	29.5344	24.8980
N VII	24.7793,24.7847	20.9095,20.9106		
O VII	21.6020	21.8071	22.1012	18.6270
O VIII	18.9671,18.9726	16.0055,16.0067	15.1760,15.1765	14.8205,14.8207
Ne IX	13.4471	13.5529	13.6988	11.5467
Ne X	12.1321,12.1375	10.2385,10.2397	9.7080,9.7085	9.4807,9.4809
Mg XI	9.1688	9.2312	9.3144	
Mg XII	8.4192,8.4246			
Si XIII	6.6480	6.6883	6.7404	
Fe XVII	15.0150	15.2621	16.7778	& 2 others
Fe XVIII	14.2030,14.2078	14.2566	14.3740	& 7 others
Fe XIX	13.5180,13.4970	15.0790,15.1976		
Fe XX	12.8172,12.8274			
Fe XXI	12.2850	12.3975		
Fe XXII	11.7700			
Fe XXIII	10.9810,11.0190	12.1610		
Fe XXIV	10.6190,10.6630	11.0290,11.1760	11.4263	

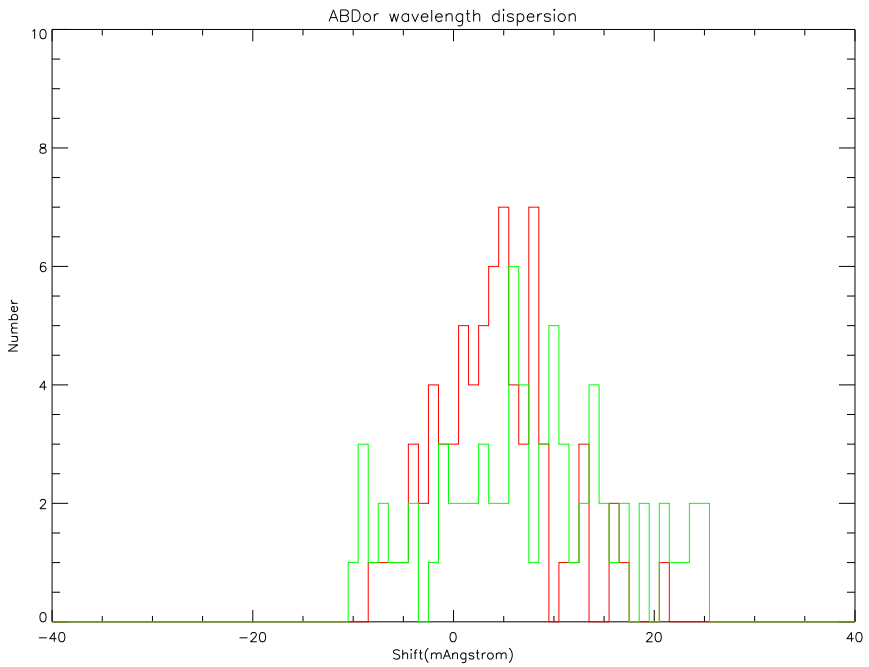

Figure 30: The distribution of wavelength shifts $\Delta\lambda = \lambda_{\rm observed} - \lambda_{\rm laboratory}$ in mÅ for the 18 ions used to model the RGS spectra of 4 observations of AB Dor. RGS1 is shown in red and RGS2 in green.

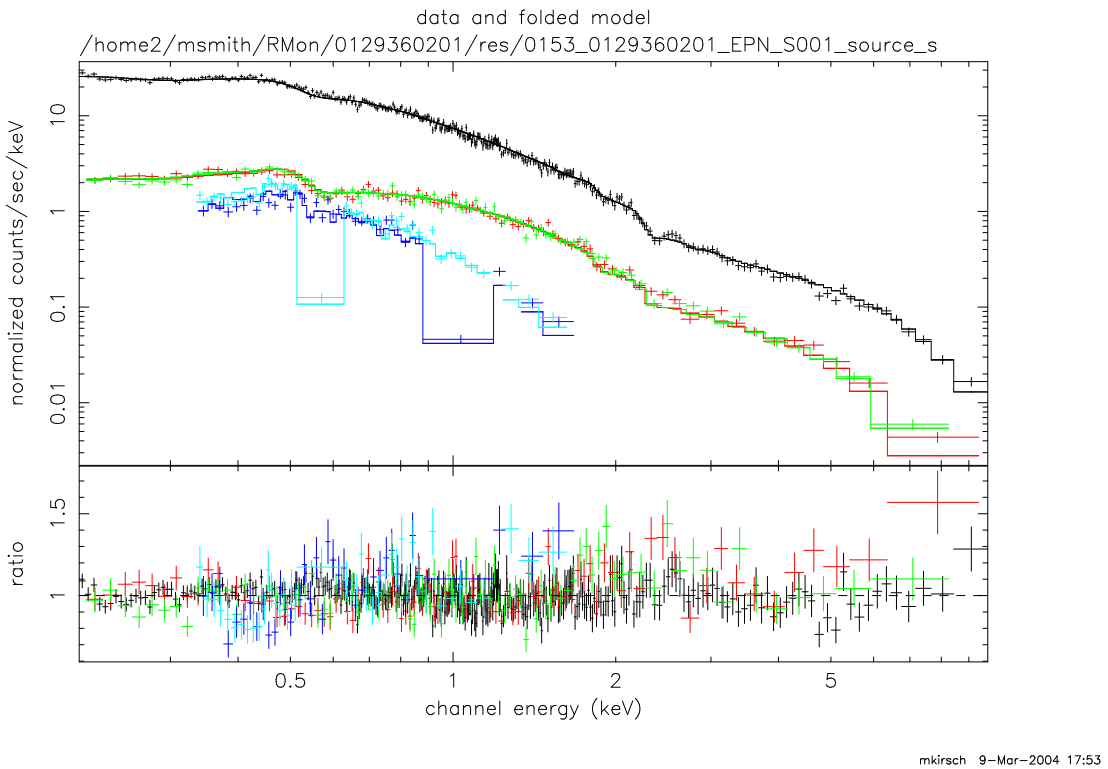

Figure 31: Spectra of PKS0558-504 with all EPIC X-ray instruments

instruments: pn: S004, MOS1: S004, MOS2: S006, RGS1: S010, RGS2: S011. Since the source was found to be variable during the observation we restricted the analysis to the time interval in which all instruments operated simultaneously between 2000-10-10T01:48:53 and 2000-10-10T03:46:38. Based on recent literature, the SIMBAD coordinates of this object have been revised by more than 12″ but we ignored this change in specifying the RGS source coordinates and used the observation pointing values given above which correspond closely with the detected EPIC position.
We used the following extraction regions (source and background, respectively):

MOS1: `((X,Y) IN annulus(25818.2,25927,174,2175)),`
`((X,Y) IN circle(23012,37410.5,4567.5))`

pn: `((X,Y) IN circle(25796.5,26014,739.5)),`
`((X,Y) IN circle(22273,29015.5,739.5))`

RGS: default `rgsproc` settings with the observation's pointing coordinates.

Spectra were extracted using single and double events, neglecting events at CCD borders and events lower than 0.15 keV. All ARFs and RMFs were generated using SAS v6.0. The spectra were modeled by a photoelectrically-absorbed combination of power-law and blackbody, allowing overall free normalization of the instruments by using a constant.
Fig. 31 shows a plot of PKS0558-504 (data and model) of the best fit to all spectra. The best-fit parameters and results are summarized in Tab. 14. Again, these number are quoted as a reference for this specific observation. Experience has demonstrated that the flux cross-normalization of the XMM-Newton instruments is dependent on the intrinsic source spectral

Table 14: PKS0558-504 best-fit parameters

Instrument	Γ	N_Γ [a]	N_H $(10^{20} cm^{-2})$	kT_{BB} (eV)	N_{BB} (10^5)	*const*	χ^2/ dof
pn	3.02 ± 0.03	$8.89 \pm^{0.09}_{0.08}$	5.93 ± 0.02	1.50 ± 0.08	9.3 ± 0.5	1	864/601
MOS1	[b]	[b]	[b]	[b]	[b]	0.93 ±0.02	...
MOS2	[b]	[b]	[b]	[b]	[b]	0.93 ±0.02	...
RGS1	[b]	[b]	[b]	[b]	[b]	0.80 ±0.02	...
RGS2	[b]	[b]	[b]	[b]	[b]	0.82 ±0.02	...

[a] in units of 10^{-3} $ph.(keV)^{-1} cm^{-2} s^{-1}$ at 1 keV
[a] linked to pn

shape. Users are referred to the calibration documentation for an updated description of the cross-calibration status.

7 Conclusions

The main conclusions of the SAS v6.0 SV can be summarized as follows:

- SAS can process all existing commissioned instrument mode (see Appendix A)
- data reduction and analysis with SAS v6.0 reproduces expected calibration accuracies as from the current calibration status
- SAS v6.0 provides for the first time reduction and analysis tools of OM exposures with the grism "filters" (although they are not processed by PPS yet)

References

Kirsch M., et al., 2004, "Proceedings of SPIE Volume: 5165, X-Ray and Gamma-Ray Instrumentation for Astronomy XIII", Flanagan K.A., Oswald H. S. eds., 85
Lehmann I., et al., 2001, A&A, 371, 833
Lorente R., et al., XMM-SOC-CAL-TN-0041, 23 July 2003
O'Brien P.T., et al., 2001, A&A, 365, L122
Tedds J. & Watson M., SSC-LUX-TN-0060, Issue 1.0, 13 November 2001
Warwick R.S., et al., 2001, A&A, 365, 248

Acknowledgments

Careful reading and useful suggestions by M.Freyberg, P.Rodriguez-Pascual, J.W. der Herder, and M.Watson are gratefully acknowledged. This report would have been impossible without the dedicated and competent support by the XMM-Newton SOC S^3T. In particular, it is a pleasant duty to mention the crucial contribution given by J.Hoar, A.Ibarra, and E.Ojero.

Appendix A: Matrix of supported instrument modes by SAS v6.0

In Tab. 15 we show the list of science instrument modes which can be processed by the SAS, and are currently being routinely processed by the pipeline.

Table 15: XMM-Newton instrument scientific modes supported by the SAS and the PPS

Mode	Processed by SAS?	Processed by PPS?
	MOS	
Full Frame	Y	Y
Large Window	Y	Y
Small Window	Y	Y
Timing Uncompressed	Y	Y
	pn	
Full Frame	Y	Y
Large Window	Y	Y
Small Window	Y	Y
Fast Timing	Y	Y
Fast Burst	Y	Y
Extended Full Frame	Y	Y
	RGS	
Spectroscopy	Y	Y
	OM	
Image Mode	Y	Y[a]
Fast Mode	Y	Y[a]
Full Frame Low Resolution	Y	Y[a]
Full Frame High Resolution	Y	Y[a]
Science User Defined	Y	Y[a]

[a]except for exposures taken in optical and UV grism

Appendix B: *Can*s and *Can't*s for SAS v6.0

This page provides a quick summary of what can and what can't be done with the SAS version discussed in this document. Moreover, it summarizes the status of the PPS data product processing.

- What SAS can do now (in brackets the SAS module responsible for the task)
  - run tasks either from the command line or through the interactive GUI
  - create script and session logs
  - create Calibration Index Files tailored to the user analysis conditions (`cifbuild`)
  - apply barycentric corrections (barycen)
  - With EPIC data
    - generate calibrated event lists (`e[mp]proc`, `e[mp]chain`)
    - extract scientific products (light curves, spectra, images) for all instrumental modes (`evselect`, `xmmselect`) from event lists. Event lists can be filtered by the user (`selectlib`).
    - run source detection algorithms on images (`edetect_chain`)
    - create Good Time Intervals from time-varying data (`tabgtigen`) and apply them to the scientific product extraction
    - create response matrices (*arfgen*; `rmfgen`) for all modes, both for point-like and extended sources
  - With RGS data
    - generate calibrated event lists (`rgsproc`)
    - run the reduction meta-task (`rgsproc`) from different entry points and to different end levels
    - extract source and background 1st and 2nd order spectra (`rgsspectrum`; run automatically through `rgsproc`)
    - create customized source lists or modifying existing EPIC source lists (`rgssources`) for scientific product extraction
    - produce plots of the dispersion versus cross-dispersion and energy versus dispersion planes, to verify the quality of the foreground and background extraction regions (`rgsimplot`).
    - generate a response matrix for a given source spectrum (`rgsrmfgen`)
    - create first- and second-order fluxed spectra (`rgsfluxer`)
  - with OM data
    - produce flat-fielded geometrically-corrected sky images for all lenticular filters, both for individual windows and for all windows combined, using image mode data
    - produce for individual windows and all windows combined, source lists, including color information for all lenticular filters using fast and image mode data
    - produce light curves time-series using fast mode data
    - produce tracking history information

    * extract wavelength and flux-calibrated OM grism spectra (`omgchain`, `omgsource`)

- What SAS cannot do yet
  - create RGS exposure-corrected light curves
  - automatically create RGS spectra (and the corresponding response matrices) for extended sources
- Which PPS Data Products are available
  - EPIC
    * Exposure and observation images and image plots
    * Exposure maps and sensitivity images
    * Exposure and observation source lists
    * Calibrated and flagged event lists
    * Flare background time-series
    * HTML summaries
  - OM
    * Science window detector sky images and image plots
    * Observation source lists
    * Tracking star time series and history plots
    * Mosaiced filter-specific images and image plots
    * Fast Mode source time-series
    * HTML summaries
  - RGS
    * Spatial and energy-wavelength images and plots
    * Exposure maps
    * Calibrated and flagged event lists
    * Source lists
    * First- and second-order source and background spectra and spectral plots
    * Flare background time-series
    * First-order response matrices
    * HTML summaries
  - General
    * HTML ODF and PPS summaries
    * PPS script log, product indices
    * Calibration index files and attitude time series

Users are reminded that exposures with not scientific filters (*e.g.*: EPIC CAL_CLOSED, OM BLOCKED) are not intended to be processed by the PPS. OM grism data are currently not processed by the PPS.